

UCSF

UC San Francisco Electronic Theses and Dissertations

Title

Adaptation of the Dynamin Fission Machine to Mitochondria in DRP1

Permalink

<https://escholarship.org/uc/item/2zz366gr>

Author

Thomas, Paul Varghese

Publication Date

2022

Peer reviewed|Thesis/dissertation

Adaptation of the Dynamin Fission Machine to Mitochondria in DRP1

by
Paul Thomas

DISSERTATION
Submitted in partial satisfaction of the requirements for degree of
DOCTOR OF PHILOSOPHY

in

Biophysics

in the

GRADUATE DIVISION
of the
UNIVERSITY OF CALIFORNIA, SAN FRANCISCO

Approved:

DocuSigned by:
ADAM FROST ADAM FROST
1E2FF75D7B5A48F... Chair

DocuSigned by:
Natalia Jura Natalia Jura

DocuSigned by:
Patrick O'Farrell Patrick O'Farrell
ACD62FEECE974F7...

Committee Members

Copyright 2022
by
Paul Varghese Thomas

Acknowledgments

I have enjoyed the opportunity to learn from such a great number of people during my PhD and will surely fail to do justice to the gratitude I feel in this acknowledgment.

First, I would like to thank Henry Nguyen, Arthur Melo, and Sasha Dickinson who have served as thoughtful and supportive scientific, career, and life mentors during my time here. Alongside them, Lakshmi Miller-Vedam, Alexander Myasnikov, Ming Sun, and Nicole Poweleit all played crucial roles in my electron microscopy training for which I am extremely grateful. I would like to thank, Bettie Osuna and Rachel DiSanto, both of whose dedication to their science served as an inspiration to me, but never kept them from always being a supportive presence. My rotation mentors, Raghav Kalia and Evan Green, have continued to offer me surprising insights throughout my PhD. I am indebted to Sasha Dickinson for hosting me at his facility in Austin which, along with Caleigh Azumaya, Eric Tse, Axel Brilot, and David Bulkley, provided me the confidence to take my next scientific and career steps. I could not have done much of the work here without the cheery and expert assistance of Loan Doan who has helped me continuously through this project.

I would be remiss to not mention Nat Hendel, Pooja Suresh, and Justin Biel who joyfully provided respite in the Sunset throughout grad school and especially during 2020. I am additionally thankful for the company and support of my friends Conor Howard, Cristina Puchades, Caleigh Azumaya, Sergei Pourmal, and Sasha Dickinson towards the end of my PhD. Of course, I must thank my close college friends José Jesus Gomez, III, Colin Nangle, Nina Randorf, Andrea Matsumoto, Irwin Tejada, Ramiro Alvarez, and Radha Arghal for keeping me grounded over the past years. I have felt incredibly lucky to have shared this period of my life

with two great friends, Hannah Yung and Karl Dunkle-Werner, whom I've now known for near half my life.

I would like to thank two of my previous scientific mentors. Dr. R. Keith Duncan and Dr. M. Gordon Joyce who provided what I now realize to be incredible mentorship and training environments and inspired a fascination with cellular machines.

Finally, I must thank Daniel Asarnow, who taught me the computational skills to build and access the infrastructure I needed to complete this project and has always been a thoughtful and curious mind that I will forever associate with my PhD experience.

Adaptation of the Dynamin Fission Machine to Mitochondria in DRP1

Paul Varghese Thomas

Abstract

The family of dynamin fission proteins polymerize and use GTP to divide eukaryotic membranous structures including endocytic necks, peroxisomes, mitochondria, chloroplasts, and plastids. Current models for how fission dynamins constrict and divide membranes describe cleavage of budding endocytic vesicles. However, the mechanisms by which dynamins can divide the larger, low-curvature membranes of entire organelles remain poorly understood. Here we report cryo-EM structures of polymers of the human mitochondrial fission dynamin-related protein 1 (DRP1) stabilized in high- and low- curvature states at 3.5-4 Å resolution. Together these reveal the structural determinants by which DRP1 is adapted to the larger diameter of the mitochondria, and a unique mechanism of constriction that allows DRP1 to constrict low curvature membranes to the size of endocytic necks without GTP hydrolysis. These adaptations of metazoan DRP1 proteins are localized to the canonical dynamin interface 1 and the interface between the Stalk domain and the Bundle-Signaling Element. These results suggest that tuning of these two interfaces allow different members of the fission dynamin family to constrict not only endocytic necks, but also a diversity of eukaryotic membrane-bound organelles.

Table of Contents

Contributing Authors	1
Introduction	1
Results	3
Discussion	11
Methods	14
Acknowledgments	21
Author Contributions	22
References	39

List of Figures

Figure 1: Inhibition of trans-rung GTPase Dimerization Reveals GTP Binding Generates High Curvature Polymerization in DRP1 through cis-rung Interactions	23
Figure S1. The Power Stroke of DRP1	25
Figure 2: Cryo-EM Structure of High Curvature GMP-PCP bound DRP1 Polymers	26
Figure 3. MiD Receptors Block a cis-rung Polymerization Interface between the BSE and the Stalk	28
Figure 4: The BSE-Stalk Interface Is Sufficient for cis-rung Mediated Generation of High Curvature in the GTP state	29
Figure S2: The C-terminal BSE Charges are Determinants of Strong cis-rung Constriction	31
Figure 5. The Canonical Interface 1 of DRP1 is Adapted to the Low Curvature of Mitochondria	33
Figure S3: Conservation of Interface 1 in Dynamin Proteins	35
Figure S4: Interface 3 is the Fulcrum of Rotation in Curvature Generation	35
Figure 6. The BSE-Stalk Interaction is Sufficient to Constrict Lipid to Endocytic Dynamin Curvatures	36
Figure 7. A Model for DRP1 Constriction of Low Curvature Membranes	38

Contributing Authors

Paul V. Thomas, Arthur A. Melo, Loan Doan, Nathaniel Dempsey, Brandon Courteau, Daniel E. Asarnow, Adam Frost

Introduction

Dynamamin-related proteins are a diverse group of large, multidomain GTPases characterized by a diversity of low affinity interactions which they use to condense and polymerize to effect a variety of cellular processes (Ramachandran & Schmid, 2018; Reubold et al., 2015). The most extensively studied member of the family, endocytic dynamin (isoforms 1-3) polymerize around budding vesicle necks to catalyze membrane scission in clathrin-mediated endocytosis. In humans, the closely related dynamamin-related protein 1 (DRP1) is recruited by receptors where it polymerizes to constrict and pinch much larger organelles, namely mitochondrial tubules, as well as mitochondrially-derived peroxisomes (Fig. 1 A) (Friedman et al., 2011; Sugiura et al., 2017). In conjunction with balanced mitochondrial fusion, this process is crucial for quality control of mitochondrial and peroxisomal protein, lipid, substrates, and mitochondrial genomes. These processes form and maintain the diversity of mitochondrial morphologies in different cell types and states.

Both DRP1 and endocytic dynamins are constitutive dimers, and share a similar overall fold and domain topology, with an N-terminal GTPase domain, a discontinuous Stalk domain interrupted by a membrane binding domain, and a highly discontinuous three helix bundle, the Bundle Signaling Element (BSE) (Fig. 1 A). In addition, endocytic dynamins contain a C-terminal proline rich domain (PRD), which along with the lipid binding specificity of the Pleckstrin Homology (PH) Domain helps localize it to endocytic necks. DRP1 lacks the PRD, and in place of the PH domain, DRP1 contains a large unstructured loop called insert B or the

variable domain, due to its lack of conservation in eukaryotes and its alternative splicing. These differences may confer different lipid and receptor binding, and therefore localization. Together these domains allow for assembly of one- and two- start helices with *cis*-rung interactions driven by polymer interfaces of the stalk domain and *trans*-rung interactions driven by dimerization of the GTPase domains specific to the GTP or hydrolysis transition state (Chappie et al., 2011; Francy et al., 2017; Ingberman et al., 2005; Kalia et al., 2018; Kong et al., 2018; J. Liu et al., 2021; Mears et al., 2011).

Two prevailing models (Antonny et al., 2016) exist for the mechanism of dynamin fission, both which focus on the stabilization of the polymer by *trans*-rung GTPase dimer interactions (Fig. 1A,B) and work showing that hydrolysis is stimulated by this interaction by ~1000-fold in endocytic dynamin-1 (Chappie et al., 2010) to ~5 fold in DRP1 (Macdonald et al., 2015). The assembly-disassembly suggests that constriction happens by assembly of the polymer in a high curvature state with energy released from each binding event. As the polymer hydrolyzes GTP, the *trans*-rung interaction is lost, leading to instability of a constricted lipid membrane without the supportive protein layer, causing fission (Fig. S1). Separately, the constrictase/ratchet model incorporates a characteristic motion of the GTPase domain in response to GTP binding, termed the power stroke (Fig. S1A) (Chappie et al., 2011). In the apo- or GDP state, the GTPase domain binds the N-terminal helix of the BSE, but binding of GTP allosterically causes the end of the helix to melt, allowing the GTPase domain to swing open 50° around hinge 2, releasing the BSE, causing a subtle rotation between helices in the bundle. Upon GTP hydrolysis or release, the GTPase domain swings shut. Here the power stroke adds a stepping motion to the helix, where GTPase domains ratchet over the neighboring rung with rounds of hydrolysis, pinching until scission (Fig. S1B).

However, the constriction/ratchet model requires closure of a turn of the helix to be able to constrict the membrane. Endocytic dynamins constrict and divide endocytic necks of ~25nm inner lumen diameter (Ferguson et al., 2009; Kong et al., 2018; Park et al., 2013), requiring at least 16 dimers before closure and in vivo machines of 28-40 dimers execute fission (Antonny et al., 2016; Cocucci et al., 2014; Kong et al., 2018; Takeda et al., n.d.). DRP1 is adapted to constrict and divide at mitochondrial pre-constrictions of ~130nm inner lumen diameter (Friedman et al., 2011), requiring about 80 dimers of DRP1 for closure or 140-200 dimers to build a similar machine, complicating the model (Ganichkin et al., 2021). Separately, work on human DRP1 and the yeast ortholog Dnm1 show substantial constriction in the presence of GTP but not GMP-PCP, which is not described by the assembly-disassembly model as the constriction should come from assembly and hydrolysis would only be required for disassembly and fission. We hypothesized that DRP1 may be adapted to use energy from GTP binding or hydrolysis towards *cis*-rung conformational changes to constrict membranes by generation of high curvature.

Results

To understand whether DRP1 has been adapted to use GTP to fuel constriction through *cis*-rung interactions, we aimed to inhibit *trans*-GTPase dimerization. The amino acid substitution D180A in endocytic dynamin-1 was shown to inhibit this interface (Chappie et al., 2010); but the equivalent D190A in DRP1 proved challenging to purify well enough for structural studies. The crystal structure of a GTPase-BSE fusion of DRP1 showed that D221 stabilizes the *trans*-GTPase dimerization interface by stabilizing the *trans*-GTPase domain's bound nucleotide (Fig. 1 B) (Kalia et al., 2018; Kishida & Sugio, 2013). This interaction is well conserved in fission dynamins but not in fusion or viral restriction dynamins. A similar GTPase-BSE fusion of DRP1 as the crystal construct was expressed and purified with and without

D221A. Negative-stain electron microscopy and size-exclusion chromatography (SEC) revealed that both wildtype and D221A GTPase-BSE fusions were monomeric in the apo state (Fig. 1 C, D). The GDP-AIF4 transition state mimetic has previously been found to be the most stable nucleotide state for *trans*-GTPase interactions. Indeed at 80 μ M *trans*-GTPase dimers were visible by negative-stain EM and by SEC for the wildtype GTPase-BSE fusion, but dimerization was severely, but incompletely inhibited by D221A. In the context of the full length DRP1, both wildtype DRP1 and D221A DRP1 formed a relatively even population of dimers and tetramers with a minority of hexamers in the GDP state at low ionic strength as visualized by negative-stain electron microscopy (Fig 1. E). Incubation with GMP-PCP led to the formation of diverse helices, presumably stabilized by the *trans*-GTPase dimer across rungs. Under similar conditions, D221A formed closed rings along with larger mixed assemblies in the GMP PCP state. Closed rings were predominantly 26- to 30-mers (13-15 dimers), indicating a GTP-dependent creation of curvature dependent on *cis*-rung interactions.

To determine what polymer interfaces and conformational changes catalyze *cis*-rung GTP dependent polymerization and generation of high curvature, we imaged these rings in vitreous ice using cryo-EM. 2D Class averages revealed that 28-mers (14-dimers) were the dominant species along with 26- and 24-mers (Fig 2. A), however averages were often focused to one side with other being blurred, perhaps due to flexibility or strain in the sample. We hypothesized that incorporation of apo-tetramers or hexamers within a ring could be adding to heterogeneity in the sample and used a disease allele G362D, which inhibits polymerization of the stalk domain to exclude any pre-formed apo-tetramers (Kalia et al., 2018). Combination of the two mutations allowed for a tighter and more stable ring sample of 24- and 26-mers (12 and 13-dimers). In a closed ring, rather than a helix, the stalk dimer axis should be, on average, orthogonal to the

polymerization axis, allowing for use of point group symmetries D1, D12 and D13, rather than helical parameters. We were able to reconstruct the 24-mer at resolution of 3.5 Å with D12 symmetry, while ~20% of the particles were 26-mers with a resolution of 4.5 Å with D13 symmetry applied (Fig 2. B). The lumen of the 24-mer has a diameter of 14nm, which is similar to the superconstricted state of endocytic dynamin (Kong et al., 2018). Importantly, mitochondria are double membraned, and therefore this constriction represents a curvature past fission of the inner mitochondrial membrane. The stalk domains were well resolved around the nominal resolution, but resolutions of the GTPase domain were poor and the unstructured insert B was not resolved. Symmetry expansion and focused alignment around an asymmetric unit revealed the closed ring to still be relatively flexible, potentially due to strain, but improved resolution of the GTPase and BSE domains to a range from high 3 Å to 6 Å.

In comparison to a published cryo-EM structure of GTP-bound DRP1 in a straight copolymer with a soluble truncation of one of its mitochondrial membrane receptors MiD49 (Fig. 3 A, B), the canonical *cis*-rung dynamin polymer interfaces 1 and 3 within the stalk domain did not show substantial changes in buried surface area (Fig. 3 C). Instead, the major difference is an interaction formed between the Bundle Signaling Element (BSE) of one protomer and the Stalk domain of another protomer on the same side of the dimer axis. MiD49 sterically blocks the formation of this interface, suggesting that MiD49 must trap DRP1 as it cycles through GTP states to form a straight (0° twist) polymer, rather than a 30° twist 24-mer ring or helix.

Although the BSE region was of lower resolution, clear density was present for a number of interleaving complimentary charges between the BSE and Stalk Domains (Fig. 4 A). At the center of these were R705 on the BSE and E433 on the Stalk Domain. Despite this interaction being GTP dependent, the GTPase domain makes almost no *cis*-rung polymeric contacts.

However, the power stroke motion of the GTPase domain allows flexibility around the GTPase-BSE Hinge, also called Hinge 2, aligning R298 of the GTPase domain to form a salt bridge with E437 of the Stalk Domain. Additionally, the GTP-dependent subtle rotation of the BSE aligns the rest of the charges and critically supports the extension of the C-terminal helix by one turn, as seen in crystal structures, allowing R705 to contribute to the interface. Moreover, the C-terminal residues, though poorly resolved, are hydrophobic and likely also contribute to the interface as the BSE buries them non-specifically against the Stalk domain. Still, this is surprising because all the residues involved in this interaction are exposed in the closed (apo or GDP) conformation.

To determine whether the BSE-Stalk interaction was necessary for ring formation, we aimed to do a charge reversal and rescue experiment. We believed that the interleaved, zipper-like arrangement of the charges on the BSE and Stalk may provide redundancy and flexibility within the interface, reducing resolution, but also complicating a single charge reversal. While the G362D D221A mutant of DRP1 sizes as a dimer in the apo state, the ring assembly was robust enough to size as a ring in the GMP-PCP state (Fig 4. B). Replacing E426R and E433R of the Stalk in this background eliminated ring formation in the open, GMP-PCP state, with the protein sizing as dimers and with no rings visible by negative-stain EM. Similarly, replacing K305E and R705E of the BSE eliminated ring formation, but did create a species larger than a dimer in both apo- and GMPPCP states. The charge reversal with all four mutations in the G362D D221A background surprisingly formed rings in both apo and GMP-PCP states by size exclusion and negative-stain EM. This suggests that R430 below E426 and E433 on the Stalk plays a role in countering the negative charge of the glutamates. Thus, the BSE-Stalk interaction would be a charge-dipole rather than a charge-charge and the overall attraction is reduced such that it can be modulated by GTP binding. To determine whether the BSE-Stalk was sufficient on

its own to drive the formation of high curvature polymerization, or if the nature of the GTPase power stroke had changed due to these mutations, we solved the cryo-EM structure of this ring at 4Å (Fig 4 C). Rather than a 24-mer, this assembly was preferentially a 22-mer, with a small number of 20-mers and 24-mers. Although the resolution of the charge reversal BSE-Stalk interaction was limited, the GTPase domain was solidly in the closed, apo-state and remained bound to the BSE (Fig 4. D), with R298 no longer involved in the interaction (Fig 4. D), indicating the power stroke was not affected by these mutations to the BSE or stalk. Instead, the high curvature generated by this charge reversal mutant implies that the wildtype BSE-Stalk interaction is likely sufficient for generating high curvature, but harnesses energy from GTP binding via the GTPase Domain power stroke. This use of GTP is described neither by the constriction by assembly model nor the constrictase/ratcheting model.

Many of these charges are conserved in endocytic dynamins (Figure S2A), and structural comparison to the helical structures of Dynamin 1 indicate that the GTPase-BSE of Dynamin 1 makes an interaction between BSE and stalk domains at Hinge 2 (Figure S2B). However, the interaction occurs with fewer complementary charges and much higher on the neighboring Stalk domain, creating a much looser Hinge 1 angle. No conserved interactions are seen in the C-terminal helix of the BSE in endocytic dynamins which contains the crucial R705. In contrast, all of the DRP1 BSE-Stalk charges are well conserved in metazoan including arthropods such as *Drosophila* and cnidarians such as the sea anemone *Nematostella vectensis*. (Fig S2C). Similar interactions are even seen in the DRP3B of *Arabidopsis* which has a mitochondrial fission phenotype and the slime mold DymA of *Dictyostelium*. These do show changes, however, including a charge reversal in DRP3B, and loss or shifting of the countercharge at the R430 position. Fungi DRP1 orthologues including *Saccharomyces cerevisiae Dnm1* stand out as

missing these C-terminal BSE interactions, suggesting the existence of other mechanisms of constriction.

The simplicity of the charge reversal experiment suggests human DRP1 has evolved to avoid constitutively making the BSE-Stalk interaction. To gain insights into an evolutionary reason for why DRP1 would not use this interaction to simply constrict by assembly, we hypothesized that removal of the GTPase and BSE domains would provide insight into other important conformations in the DRP1 constriction and fission mechanism. The Stalk Domain including insert B polymerized well at low concentrations and physiological salt, suggesting that the GTPase and BSE domains provide an autoinhibition of polymerization. These polymers had very low curvatures relative to GMP-PCP ring samples, but formed not only *cis*-rung interactions, but also *trans*-rung interactions, reminiscent of a proposed interface 4 from the crystal structure of DRP1 (Fig. 5 A) (Fröhlich et al., 2013). The *trans*-rung interactions preferentially formed two or three wide triplets of filaments, which zipped apart and together repeatedly, creating very large tangles in vitreous ice, complicating automated data collection. Surprisingly, removal of a 20 amino acid stretch of insert B with predicted helical propensity (Lu et al., 2018) and conserved in all splice variants, severely inhibited the formation of filament triplets (Fig 5 B). Residues 562-582 are also involved in lipid binding (Bustillo-Zabalbeitia et al., 2014; Mahajan et al., 2021), and contain four of the DRP1 SUMOylation sites (Figuroa-Romero et al., 2009). The resulting filaments appeared to have the same curvature as the Stalk Domain including full length insert B. We were able to solve this structure to a resolution of 3.5Å, revealing an overall twist of 5.14°, yielding a diameter of curvature of ~120nm (Fig. 4 C). This curvature is equivalent to curvatures of apo DRP1 on liposomes (Francy et al., 2017) and the yeast ortholog Dnm1 on liposomes in both apo- and GMP-PCP states (Ingerman et al., 2005;

Mears et al., 2011). While the stalks are well resolved, again insert B is not resolvable in this reconstruction, however residual density for a small number of triplets can be observed at low contours.

In comparison to the endocytic dynamin 1 2 start structure with a 26nm diameter measured at interface 3, the mostly conserved interface 1 bears intriguing similarities (Fig. 5 D). Although DRP1 stalk protein has much lower twist, the hydrophobic core formed by the side chains is closed and intact, however the position of overall position of the helices reflects the great change in diameter. Conversely, the ~20nm DRP1 24mer ring, shares similar overall helix positioning with the dynamin 1 2 start interface 1, but the hydrophobic core is pulled apart exposing V661 and breaking hydrogen bonding between Q657. Interestingly, these are the two residues that are substantially different between DRP1 and Dynamin 1 in interface 1, with Q657 in DRP1 replacing the role of Q334 in Dynamin 1 and V661 replacing the larger L702 of Dynamin 1. This indicates that the DRP1 interface 1 is adapted to form a wider preferred curvature of ~120nm or ~105nm at the inner lumen of the membrane, which better matches the diameter of the pre-constricted mitochondria. These residues are again well conserved in metazoan DRP1 orthologues, and in other eukaryotes, but the equivalent of V661 is not the same in *Arabidopsis* DRP3B (Fig. S3).

On the other hand, R403 of interface 3 forms a fulcrum of rotation and experiences minimal changes between these diverse curvatures, while interface 1 slides (Fig. S4). Additionally, the disease allele G362D in interface 3 can be determined to be replacing E359 in a basic patch formed by R365 and R441. This causes melting of a turn of the helix C-terminal to L1 and causes the L1 loop to become poorly ordered, while it has assignable side chain density and register in the absence of G362D. Membrane proximal to interface 3, a small helix at the tip

N-terminal tip of insert B, is on the other side of the interface 3 fulcrum, and while interface 1 gets pulled apart, these helices are pushed together between protomers. It is possible that these also aid in the adaptation of DRP1 to low curvature or affect the insert B conformational landscape.

The low curvature structure suggests that the BSE-Stalk interaction is used to progress from a low curvature assembly with mild constriction to a high curvature one using GTP. However, the high-curvature rings were assembled in solution without the presence of any lipid bilayer and including a mutant within interface 3 which inhibited normal polymerization. To determine whether the BSE-Stalk interaction, without any *cis*-rung interactions was sufficient for high curvature generation on lipid we imaged these proteins on nanotubes containing galactosylceramide, phosphatidylserine, and cardiolipin (Fig 6A). Unlike Dynamin 1 which can assemble helically on nanotubes in GDP states, albeit with higher rise and greater path length, wild type DRP1 and D221A coated but failed to assemble on nanotubes without GMP-PCP (Fig 6B). Surprisingly, wildtype DRP1 formed a two-start helix in the GMP-PCP state, while D221A DRP1 continued to form closed rings on the lipid, as in solution (Fig 6C.). A thin projection slice of these two samples shows *trans* GTPase dimers forming in DRP1 WT with the canonical dynamin T shape (Fig 6D), while D221A remains dense and compact, indicative of a similar GTPase domain position as the solution structure of DRP1 D221A G362D. This indicates that D221A is sufficient to inhibit *trans*-GTPase dimerization in the GMP-PCP state even at the high concentrations of polymers achieved on lipid. Additionally, the formation of rings in the absence of GTPase dimerization suggests that DRP1 stalks and insert B may have flexibility in their rise parameters. The charge reversal mutant which constitutively makes the BSE-Stalk interaction formed tight, one start helices in all states and with and without D221A, furthering the idea of

flexibility in the rise parameters for this protein. On liposomes, the D221A charge reversal mutant was unencumbered by galactosyl ceramide and constricted phosphatidylserine and cardiolipin liposomes to an inner lumen of 10nm, equivalent to the constricted state of dynamin 1. Thus, the BSE-Stalk interaction allows DRP1 to proceed with constriction of large membrane to very far in the reaction, where perhaps DRP1 begins to function similarly to endocytic dynamin and either causes scission through disassembly or the constriction/ratchet model.

Discussion

Adaptation of DRP1 and its orthologs to the low curvature of mitochondrial and peroxisomal fission sites was reported shortly after discovery of a mitochondrially acting dynamin (Francy et al., 2017; Ingerman et al., 2005; Mears et al., 2011) . Here we report the structural determinants that allow for assembly of the dynamin polymer at low curvature and a mechanism by which GTP binding and exchange is used to constrict the membrane to a curvature similar to the state of the constricted endocytic dynamin (Antonny et al., 2016; Kong et al., 2018). Overall, our results suggest a model where localization of receptors including MiD49, MiD51, MFF, and Fis-1 to the mitochondrial pre-constriction site recruits DRP1 from the cytosol (Figure 7) (Losón et al., 2013). This increase in local concentration of DRP1 allows for the formation of canonical dynamin polymerization interfaces 1 and 3, as well as DRP1-receptor interactions and lipid binding by insert B (Kalia et al., 2018). Because MiD receptors selectively bind the open, GTP-bound state of DRP1 (Kalia et al., 2018) and block formation of the GTP-dependent BSE-Stalk interaction, they must trap DRP1 between open-closed cycles. Similarly, MFF has been reported to bind the apo-state of DRP1 (Clinton et al., 2016; R. Liu & Chan, 2015) even though the dominant state of DRP1 should be GTP-bound, given GTP concentration in the cell (Ganichkin et al., 2021). However, both enzymatic and recent smFRET data indicate

that dynamins have high off-rates of GTP and subsequently cycle rapidly through open and closed states simply through binding and release, with hydrolysis being a comparatively rare event (Ganichkin et al., 2021; Macdonald et al., 2015). Most mitochondrial fission in mammals is thought to be nucleated by MFF, which has been shown to rapidly accumulate at sites of fission in response to curvature (Helle et al., 2017) by either pre-constriction from the ER (Friedman et al., 2011) or other factors. Both MiD and MFF induced polymerization of DRP1 has been remarkably straight, with infinite curvature (Clinton et al., 2016; Kalia et al., 2018) which would surprisingly exclude them from curling around the pre-constriction site (Fig. 7). By hydrolysis and release of the MiD receptor, or likely simply through cycles of opening and closing in the case of MFF, DRP1 can release from these receptors and enter into the pre-constriction site, strengthening interface 1 and allowing for greater lipid binding of the polymer (Fig. 7). This is revealed by the 5.3° twist and ~ 120 nm diameter of curvature structure reported here, which matches reports of the apo state of DRP1 and the yeast Dnm1 on liposomes (Francy et al., 2017; Ingelman et al., 2005; Mears et al., 2011) and is similar to the ~ 140 nm diameter of the preconstruction site from outer leaflet to outer leaflet (Friedman et al., 2011). This is in stark contrast to the apo state of endocytic dynamin on liposomes which would have a diameter of curvature of ~ 30 nm measured at interface 3 (Chen et al., 2012; Danino et al., 2004; Sweitzer & Hinshaw, 1998; Takei et al., 1998, 1999) which matches curvatures of the endocytic neck in dynamin knockouts (Ferguson et al., 2009; Park et al., 2013). Interestingly, this also suggests a mechanism that limits the backward step of receptor binding in the constriction site, as this would straighten the polymer and push it away from the membrane.

While endocytic dynamin also constricts upon GTP-binding, it does so relatively modestly, from a curvature of ~ 20 nm of the outer leaflet, to a curvature of ~ 17 nm of the outer

leaflet. In contrast, here we report that interactions between the BSE domain of one protomer and the Stalk domain of the neighboring protomer within the same rung of the polymer cause an intermediate constriction of the wider mitochondrial pre-constriction site of ~120nm to ~20nm at the outer leaflet (Fig. 7). The BSE-Stalk interaction harnesses energy from GTP-binding causes a weakening of interface 1, but it does not have enough binding energy on its own without the context of a pre-assembled polymer. Because of the rapid kinetics of GTP binding and release, it is likely that this constriction requires multiple openings and closings of the GTPase-BSE domains and suggests an annealing rather than a strictly mechanical use of the power stroke motion. However, GMP-PCP bound assemblies of the yeast Dnm1 on lipid have similar curvatures to the apo Dnm1 and require GTP to constrict at all (Mears et al., 2011). This is likely due to premature formation of the *trans*-GTPase domain dimerization interface across rungs of the Dnm1 helix, trapping the preferred low curvature state. Indeed, recent modeling work of endocytic dynamin shows that *trans*-GTPase dimerization can restrict the polymer from constricting, especially without the consideration of the polymer strain of mismatched *trans*-GTPase dimers that would be effectively absent at the low curvatures of apo-DRP1 (Ganichkin et al., 2021). High resolution cryo-EM structures of dynamin-1 have also illustrated that the *trans*-GTPase dimer is at odds with the BSE-Stalk interaction, and selection of stable long helices which must be *trans*-GTPase dimer dominated require trapping of one GTPase-BSE with an extreme kink in Hinge 2, between open and closed states (Kong et al., 2018; J. Liu et al., 2021). Thus, going from the ~20nm curvature of the outer leaflet we observe with a BSE-Stalk dominated assembly (Fig. 6E), a curvature similar to that of endocytic dynamin, likely requires steps where the BSE-Stalk interaction is lost to the *trans*-GTPase Dimer interface (Fig. 7). Although these interactions are stronger, they only show up at the high concentrations achieved

by closure of the helix (Chappie et al., 2010, 2011). For endocytic dynamin, we know that the fission machine is only 28-40 dimers, or 1.5-2 turns of the helix, thus for DRP1, the appropriate time for formation of *trans*-GTPase dimers is likely well after the intermediate mediate constriction dominated by the BSE-Stalk.

The numerous, low-affinity interactions that allow dynamin-family proteins to condense and polymerize to execute membrane remodeling functions has previously been discussed as “matricity” or in phase-separation or liquid-liquid demixing in modern parlance (Reubold et al., 2015; Schmid & McMahon, 2007). In these regimes, avidity is high enough that diffusion kinetics no longer describe the formation and dissociation of interactions, and low affinity interactions with favorable geometries can be highly significant (Schmid & McMahon, 2007). In the context of DRP1, a succession of polymer interactions takes place, each one with its own role in increasing local concentration and creating the geometric constraints which allow the next interaction to form, potentially breaking previous interfaces (Fig. 7). This allows for overall direction to the fission reaction, with energy for this annealing provided by polymerization, GTP binding, release, and hydrolysis. Tuning of the relative affinities and geometries of these interactions, in this case, interface 1 and the BSE-Stalk interface can therefore allow dynamin proteins to be adapted to divide a diversity of organelles, along with endocytic necks.

Methods

Protein Purification

Plasmids encoding for proteins used in this paper were transformed into LOBSTR BL21(DE3) *E.coli* (Kerafast) carrying a pRARE2 plasmid. Starter cultures were grown overnight at 37°C in LB media containing the required antibiotics. Bacteria were then grown in ZY autoinduction medium with the required antibiotics in baffled flasks for 5 hours at 37°C, then for 21 hours at

18°C. Cultures were centrifuged and cell pellets were resuspended in lysis buffer containing lysozyme and excess protease inhibitors to preserve the unstructured insert B. For DRP1 GTPase-BSE fusions, 50mM Tris, pH 8; 500mM NaCl, 10mM imidazole, and 1mM DTT was used as lysis buffer, but for all other DRP1 constructs (containing stalk domains) this was supplemented with 500mM L-arginine hydrochloride, pH 8 to reduce polymerization, 20mM sodium tripolyphosphate and 20mM sodium hexametaphosphate to reduce nucleic acid binding, 0.5mM EGTA for further reduction of protease activity, and an additional 10mM imidazole. Resuspended pellets were stirred at 4°C for 1hr to weaken cell walls before flash freezing in liquid nitrogen and stored at -80°C until later processing.

After thawing resuspended pellets, lysis and DNA clarification was completed by sonication (Active Motif EpiShear). The lysate was then centrifuged at 35,000xg and 0.45 µm filtered before flowing over pre-equilibrated Ni-NTA agarose resin (Qiagen). For GTPase-BSE fusions, the beads were washed with 10 column volumes (cv) of lysis buffer, and then 5 column volumes of lysis buffer containing 40mM imidazole before eluting in lysis buffer containing 400mM imidazole, pH 8. For all other DRP1 constructs, the beads were washed with 10cv of 50mM Tris, pH8; 500mM NaCl; 20mM imidazole; 500mM L-arginine hydrochloride, pH 8, then 5cv the same solution with an additional 20mM imidazole, then the same solution with 5cv of the same solution with 3mM MgCl₂ and 10mM ATP to remove chaperones; then 5cv of the same solution, then 5cv of the same solution containing 20mM sodium tripolyphosphate, 20mM sodium hexametaphosphate, 20mM sodium orthophosphate and 0.5mM EDTA to reduce contaminants absorbing at 260nm, then 5cv of the same solution again before eluting with the same solution containing 400mM imidazole, pH 8 and protease inhibitors to protect insert B from contaminant proteases. Proteins were concentrated and an additional 10mM EDTA, 10mM

EGTA, and 3mM DTT were added. After centrifuging any aggregates and 0.1 μ m filtering protein, DRP1 GTPase-BSE fusions were separated by size-exclusion chromatography on a Superdex 75 Increase 10/300 GL column (Cytiva) in 20mM HEPES, pH 7.5, 120mM NaCl, 3mM MgCl₂, 1mM DTT. For all other DRP1 constructs, protein was separated by size-exclusion chromatography on a Superdex 200 Increase 10/300 GL (Cytiva) in 10mM HEPES, pH 7.5; 300mM NaCl, 1mM TCEP, and 200mM L-arginine hydrochloride to inhibit oligomerization of DRP1. Only the peak corresponding to a DRP1 dimer was collected and used for later experiments since removal of arginine rapidly returns full length DRP1 to an equilibrium of hexamers, tetramers, and dimers. All DRP1 proteins used in this paper are based on DRP1 isoform 2 and use isoform 2 numbering (Uniprot O00429-3).

Soluble MiD49 (residues 126–454) and soluble MiD51 (residues 132–463) were expressed as described above and purified as previously described (Kalia et al., 2018), except that overnight, on-column HRV-3C cleavage was used in both cases to separate GST from MiD proteins using a large excess of GST beads. MiD proteins were collected in resin flow through and washes before concentrating and sizing as previously described.

DRP1 GTPase-BSE Fusion Dimerization Assay

DRP1 GTPase-BSE fusion proteins were incubated at 37°C for 30 min at concentration of 80 μ M in 20mM HEPES, pH 7.5; 120mM sodium chloride, 3mM magnesium chloride, 20mM sodium fluoride, and 2mM aluminum chloride with 2mM GDP for GDP-AlF₄ samples or no GDP for apo samples. A reaction sample was diluted to a concentration of 5-20 μ g/ml for negative-stain electron microscopy and approximately 400 μ l of the reaction was 0.1 μ m filtered and purified by size exclusion chromatography on a Superdex 75 Increase 10/300 at 10°C in 20mM HEPES, pH

7.5; 120mM sodium chloride, 3mM magnesium chloride, 20mM sodium fluoride, and 2mM aluminum chloride. Care was taken to use freshly filtered buffer as solutes would precipitate from solution over time, presumably due to fluoridation of buffer components.

Assaying Ring Assembly by Size-Exclusion Chromatography

DRP1 G362D D221A backgrounds were used due to the ability of apo- DRP1 G362D D221A to size monodispersely as a dimer in a variety of ionic conditions, while DRP1 D221A can form small oligomers in the absence of nucleotide and while G362D can form G-G interactions in the presence of GMP-PCP, confounding size exclusion assays. Proteins were diluted to 0.5mg/ml (6 μ M) in 10mM HEPES, pH 7.5; 300mM sodium chloride, 20mM potassium chloride, 3mM magnesium chloride, and 0.5mM TCEP and dialyzed against 10mM HEPES, pH 7.5; 60mM potassium chloride, 40mM sodium chloride, 6mM magnesium chloride, 1mM TCEP, and 5% glycerol with or without 200 μ M GMP-PCP at room temperature overnight. A reaction sample was diluted to a concentration of to 50 μ g/ml for negative-stain electron microscopy and approximately 400 μ l of the reaction was 0.1 μ m filtered and purified by size exclusion chromatography on a Superose 6 Increase 10/300 in 10mM HEPES, pH 7.5; 60mM potassium chloride, 40mM sodium chloride, 6mM magnesium chloride, 1mM TCEP, and 5% glycerol with or without 200 μ M GMP-PCP at room temperature.

Ring Assembly for Electron Microscopy

His-tagged DRP1 G362D D221A was diluted to 0.5mg/ml (6 μ M) in 10mM HEPES, pH 7.5; 300mM sodium chloride, 20mM potassium chloride, 3mM magnesium chloride, and 0.5mM

TCEP and dialyzed against 10mM HEPES, pH 7.5; 25mM potassium chloride, 6mM magnesium chloride, 1mM TCEP, and 1% glycerol with 300 μ M GMP-PCP at room temperature overnight. An additional 400 μ M GMP-PCP was added before freezing the assemblies on lacey carbon grids (LC300-Au-150) using a Thermo Scientific Mark IV Vitrobot at 100% humidity. Grids were plunge frozen after 20 seconds of sample contact time and 4 or 8 seconds of blotting with Whatman #1 paper and Blot Force 0-1. His-tagged DRP1 G362D D221A E426R E433R K305E R705E assemblies were prepared similarly, but without any GMP-PCP included.

Stalk Assembly for Electron Microscopy

His-tagged DRP1 stalk and variable domain proteins (residues 324-678, DRP1 isoform 2) were diluted to 3-5 μ M in 10mM HEPES, pH 7.5, 1mM TCEP with 0.5M NaCl or 1M L-arginine HCl for a final volume of 100 μ l. For cryo-EM 1% glycerol was also supplemented. The diluted sample was then dialyzed against 13.5ml of 10mM HEPES, pH 7.5; 25mM KCl, 3mM MgCl₂, 1mM TCEP, and 1% glycerol for 3 hours to overnight. For Δ 562- Δ 582 stalks, His-tagged DRP1 stalk and variable domain proteins (residues 324-678 Δ 562-582, DRP1 isoform 2) were not treated with arginine and instead were either diluted to a 5 μ M in 10mM HEPES, pH 7.5; 100mM KCl, 0.5mM TCEP for 3 hrs and frozen on lacey carbon grids (LC300-Au-150) or the protein was diluted to 10 μ M in 10mM HEPES, pH 7.5; 100mM KCl, 1mM DTT for approximately 30 min and frozen on Copper 400 mesh R1.2/1.3 grids Grids were plunge frozen after 20 seconds of sample contact time and 4 or 8 seconds of blotting with Whatman #1 paper and Blot Force 1-2.

Negative-stain Electron Microscopy

Samples were diluted with the matching buffer to a concentration appropriate for visualization and/or averaging and applied to glow discharged homemade negative-stain grids before staining with 0.75% uranyl formate. Images were recorded on either a Phillips T12 or T20 electron microscope equipped with either a Gatan Rio or Tietz TVIPS camera. Two-dimensional classification and averaging was conducted using cryoSPARC (Punjani et al., 2017) versions 2.3-3.3..

Single Particle Electron Cryo-microscopy

Data was collected using SerialEM 3.7-3.8 (Schorb et al., 2019) on Titan Krios G3 microscopes with Gatan K3 direct electron detectors and either a prototype or a production Gatan BioQuantum K3 Energy Filter at a magnification of 105kX. Initial processing was done in cryoSPARC (Punjani et al., 2017) v3.2 with further processing done in RELION 3.0.8 (Zivanov et al., 2018) and 3.1.x (Zivanov et al., 2020) and cisTEM-1.0.0-beta (Grant et al., 2018) with frequent use of pyEM (Asarnow et al., 2019) for data and metadata conversion. Platonic rings roughly matching the dimensions seen in 2D averages were made in SPIDER⁶ or ChimeraX (Goddard et al., 2018; Pettersen et al., 2021) were used as initial references for 3D processing until a library of 10-14mer reconstructions of varying resolutions were eventually classified from various datasets and combinations thereof were used for initial angles and for classifications. For 3D processing of constructs without the GTPase and BSE domains, a stalk domain tetramer from PDB ID 5WP9 (Kalia et al., 2018) with a low pass of 30Å was used as an initial reference. Modeling was done using *Coot* (Emsley et al., 2010; Emsley & Cowtan, 2004) and ISOLDE (Croll, 2018; Pettersen et al., 2021) within ChimeraX (Goddard et al., 2018; Pettersen et al.,

2021), followed by PHENIX (Liebschner et al., 2019) using recommended options (Tristan Croll, 2021). Structures were visualized and analyzed using ChimeraX (Goddard et al., 2018; Pettersen et al., 2021) and PyMOL (Schrödinger, LLC, 2015) as well as PISA (Krissinel & Henrick, 2007).

Assembly of DRP1 Polymers on Lipid Nanotubes

A 5mg/ml stock solution of Gal-Cer (D-galactosyl- β -1,1' N-nervonoyl-D-erythro-sphingosine (Avanti 860546-5mg) was prepared in 1ml of 20:9:1 chloroform:methanol:water (v/v/v) (Avanti 690014).

Nanotubes comprised using 50% Gal-Cer, 30% POPS, and 20% cardiolpin were made by mixing 500 nmol Gal-Cer (Avanti 860546P) (81 μ l 5mg/ml Gal-Cer stock), 300 nmol POPS (Avanti 840034C) (23 μ l 10mg/ml stock), and 200 nmol cardiolipin (Avanti 710335) (30 μ l of 10mg/ml stock) in a 5ml Thermo Reactivial. The mixture was heated to 50°C and sonicated at 100% power at 37kHz in a bath sonicator for 5 minutes to make sure Gal-Cer mixed with other lipids. The solution was dried under nitrogen gas while vortexing to form a thin layer. The thin layer was resuspended in 300-500 μ l of chloroform and heated and sonicated again for 5 minutes. The solution was dried under nitrogen gas while vortexing to form a thin layer and residual chloroform was allowed to dry out in a vacuum dessicator for at least 2 hours.

The mixture was resuspended in 623 μ l of 20mM HEPES, pH 7.5; 150mM KCl, 1mM TCEP for a final concentration of 1.5 mg/ml lipid and vortexed gently before heating to 50°C and sonicated at 100% power at 37kHz in a bath sonicator for 5 minutes. The solution was pipetted up and down while scraping the sides with vortexing to get all lipid off the walls and in solution before heating and sonicating again for 5 minutes. Nanotubes were then extruded through a 0.2 μ m filter.

Nanotubes were diluted as quickly as possible to 0.5 mg/ml with 6 μ M (0.5 mg/ml) DRP1 protein. Samples were dialyzed against the desired ionic strength for 1hr. If indicated, nucleotide was added to the dialysis solution after 1 hr of dialysis to make sure DRP1 assembled only on the membrane and not in solution. After 3 hours total, an additional 100 μ M of nucleotide was added to the protein and nanotube reaction and removed from dialysis before negative-stain or cryo-EM.

Electron Cryo-tomography of DRP1 Polymers on Lipid Nanotubes

Cryo-tomograms were collected using Serial-EM and processed using Dynamo, IMOD, and IsoNet. Models were made using blender to match the original density.

Acknowledgements

We thank David Bulkley, Glen Gilbert, Eric Tse, Alex Myasnikov, and Zanlin Yu for their maintenance and service of the electron microscopy facility at UCSF. We thank Ming Sun, Nicole Poweleit, and Henry Nguyen for their thoughtful support in electron microscopy and Henry Nguyen, M. Sasha Dickinson, Alex Brilot, Daniel Asarnow, and Ming Sun for their thoughtful discussion on cryo-EM data processing. We thank Joshua Baker-LePain and the Wynton HPC team for development, maintenance, and support of UCSF HPC resources. We also thank Lakshmi E. Miller-Vedam, Arthur Melo, and Halil Aydin for thoughtfully providing computational resources. Structural biology applications used in this project were compiled and configured by SBGrid. This study was supported by NIH (no. 5R01GM127673 and 5T32GM008284-33.). Adam Frost was further supported by a Faculty Scholar grant from Howard Hughes Medical Institute and was supported as a Chan Zuckerberg Biohub investigator.

Author Contributions

P.V.T: Conceptualization, Methodology, Validation, Formal Analysis, Investigation, Resources, Data Curation, Writing- Original Draft Preparation, Writing – Review and Editing, Visualization, Supervision, Project Administration, Funding Acquisition

A.M: Conceptualization, Methodology, Validation, Formal Analysis, Investigation, Resources, Data Curation, Writing- Original Draft Preparation, Writing – Review and Editing, Visualization, Supervision, Project Administration, Funding Acquisition

L.D.: Methodology, Investigation, Resources, Writing – Review and Editing, Project Administration

D.E.A.: Methodology, Software, Formal Analysis, Writing – Review and Editing

B.C.: Formal Analysis, Investigation, Writing – Review and Editing

N.D.: Formal Analysis, Investigation, Writing – Review and Editing

A.F.: Funding Acquisition, Writing –

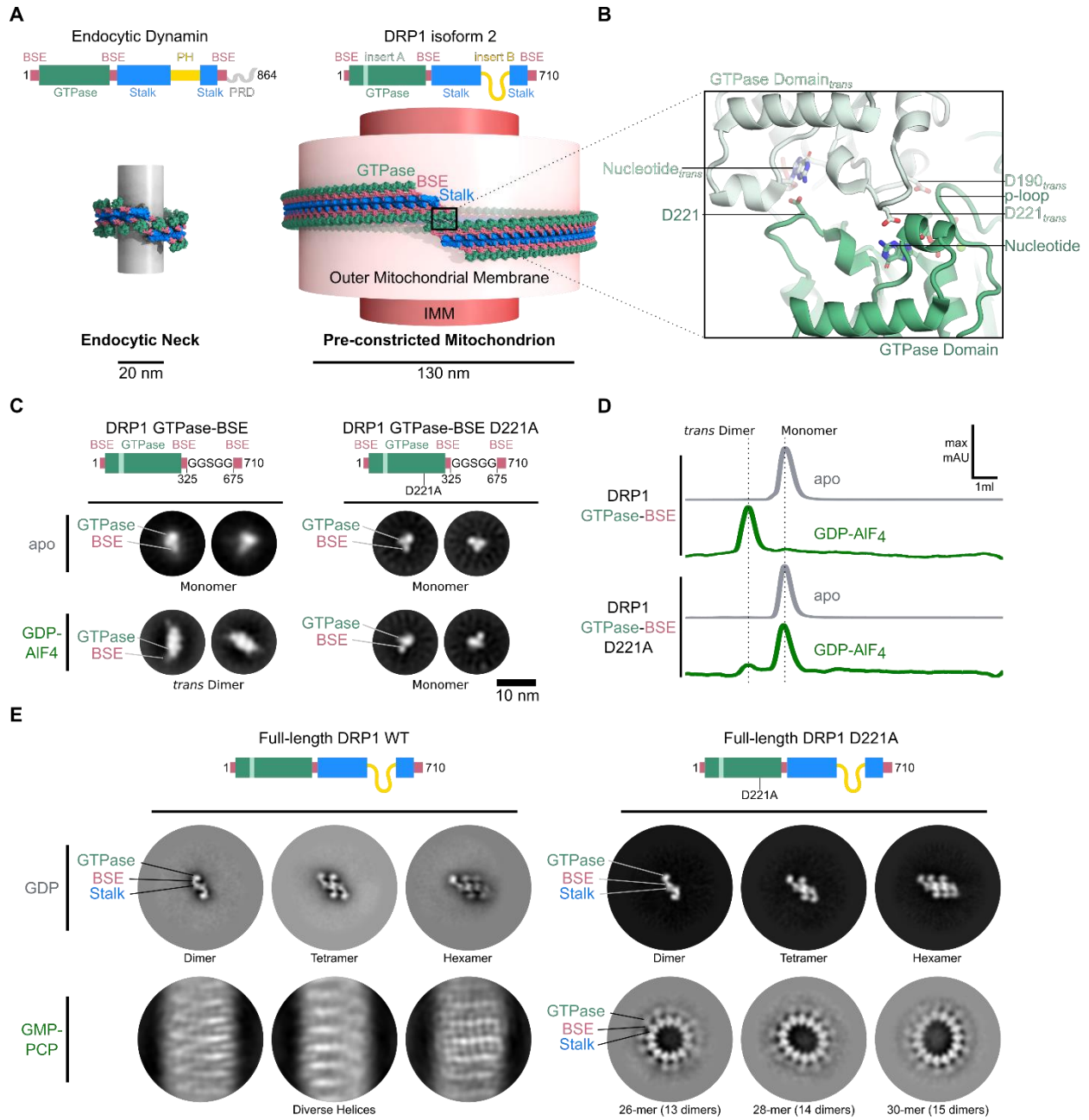


Figure 1. Inhibition of trans-rung GTPase Dimerization Reveals GTP Binding Generates High Curvature Polymerization in DRP1 through *cis*-rung Interactions

(A) Domain organization of endocytic Dynamin 1 and DRP1 isoform 2 in primary sequence and in the context of a polymer on their respective target membranes. PDB 6DLU of the one-start constricted Dynamin 1 on membrane was used for endocytic dynamin, while a model based on the dimer of 5WP9 was used for DRP1. Diameters of target membrane refer to the luminal diameter from inner leaflet to inner leaflet. Domains colored according to the sequence diagram. (B) Structure of the DRP1 trans-GTPase dimer interface from the crystal structure of the DRP1 GTPase-BSE fusion in the GMP-PCP state (PDB 3W6O) with one monomer in dark green and the other in pale green. (C) Sequence Diagram of the GTPase-BSE construct used for negative-stain EM and (D) size-exclusion assays of trans-GTPase dimerization in the presence and absence of the transition state mimetic GDP-AIF4 and in the context of the wild type GTPase Domain or D221A and subsequent results. (E) Sequence diagrams and negative-stain EM of full-length DRP1 isoform 2 with and without D221A in the presence of either GDP or GMP-PCP under low ionic strength conditions without lipid.

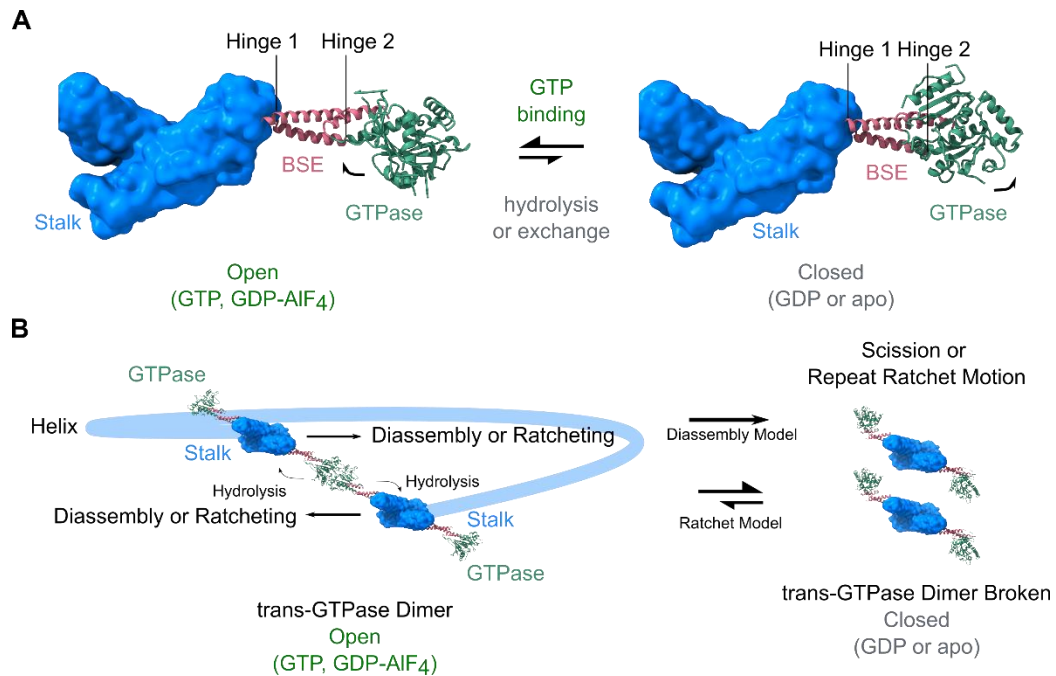


Figure S1. The Power Stroke of DRP1

Comparison between the closed state (apo or GDP) of DRP1 using the PDB 4BEJ which structure and a model of the open state using the GTPase-BSE of PDB 3W60 aligned to the BSE of PDB 4BEJ. PDB 4BEJ is the crystal structure of the GTPase, BSE, and most of the Stalk Domain of DRP1 with mutations in the stalk to inhibit polymerization and removal of the unstructured insert B and the sequence immediately N-terminal to insert B. (B) The Power Stroke of DRP1 in the context of trans-rung GTPase dimer stimulated hydrolysis in constriction by assembly-fission by disassembly and constriction/ratchet models.

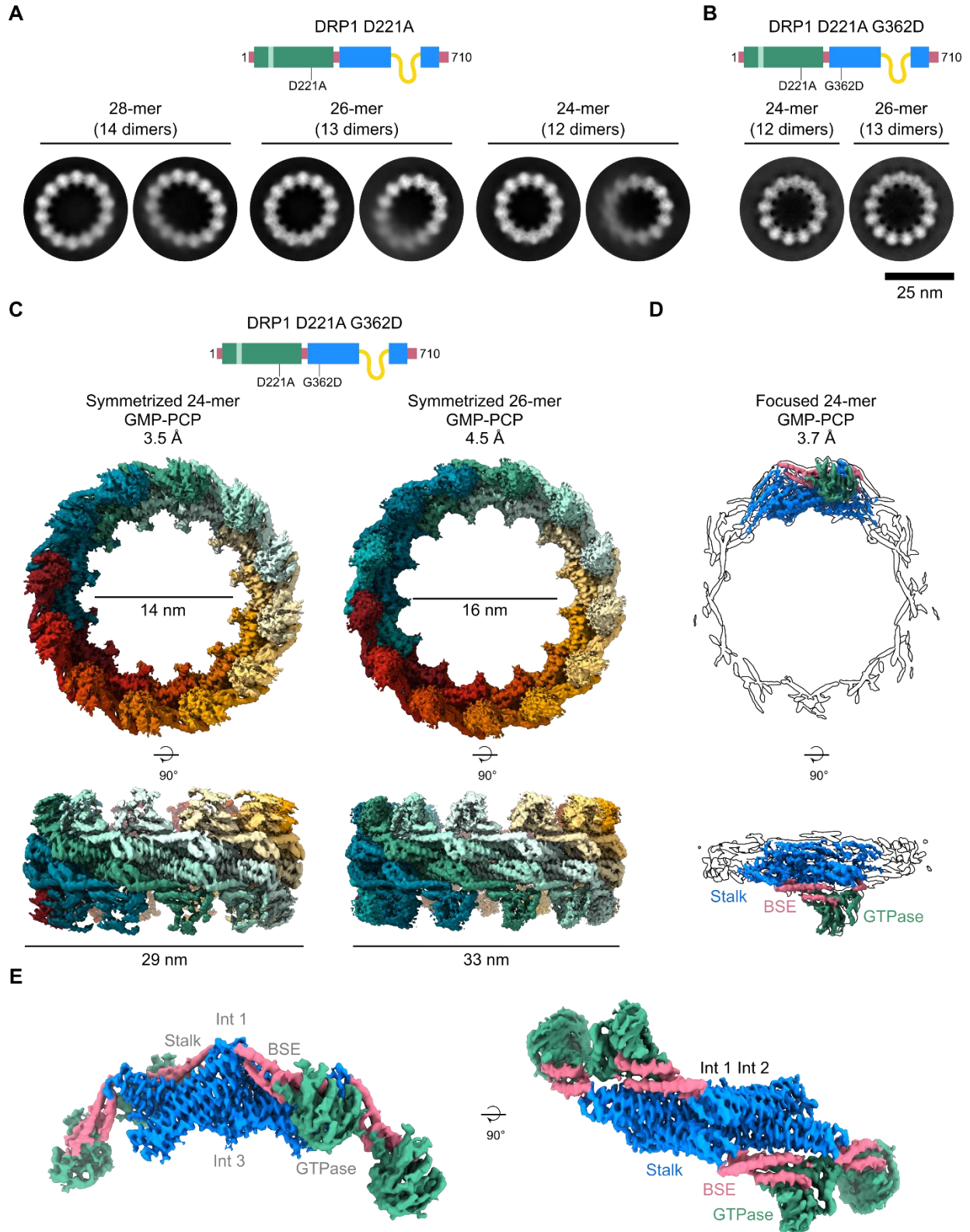


Figure 2. Cryo-EM Structure of High Curvature GMP-PCP bound DRP1 Polymers

(A) Sequence Diagram and 2D averages of GMP-PCP bound DRP1 D221A in vitreous ice under low ionic strength conditions, with better averaged closed rings on the left and poorly averaged rings on the right for each species. Scale bar, same as in (B) Sequence Diagram and 2D averages of GMP-PCP bound DRP1 D221A G362D closed ring assemblies in vitreous ice under low ionic strength conditions with one average per observed species. (C) Symmetrized 3D cryo-EM reconstructions of GMP-PCP bound DRP1 D221A G362D 24 and 26-mer closed rings frozen at low ionic strength conditions at nominal resolutions of 3.5Å and 4.0Å with each constitutive dimer colored a different color. (D) 3D cryo-EM reconstruction of the symmetry expanded 24mer of DRP1 D221A G362D with alignment focused on the GTPase, BSE, and nearest stalk domain on one side of the dihedral axis. The unmasked map at low threshold is colored according to the sequence diagram in (B, C) and silhouettes of the map are shown at medium threshold, showing correlation between stalks across the dihedral dimer axis, and some correlation between a GTPase-BSE and its own stalk and little correlation in the ring overall. (E) The GTPase-BSE density of the focused map aligned to and replacing the GTPase-BSE densities of the symmetrized map to show the canonical polymerization interfaces 1 and 3 and the dimer interface 2. The stalk domain was kept from the symmetrized map as it is higher resolution.

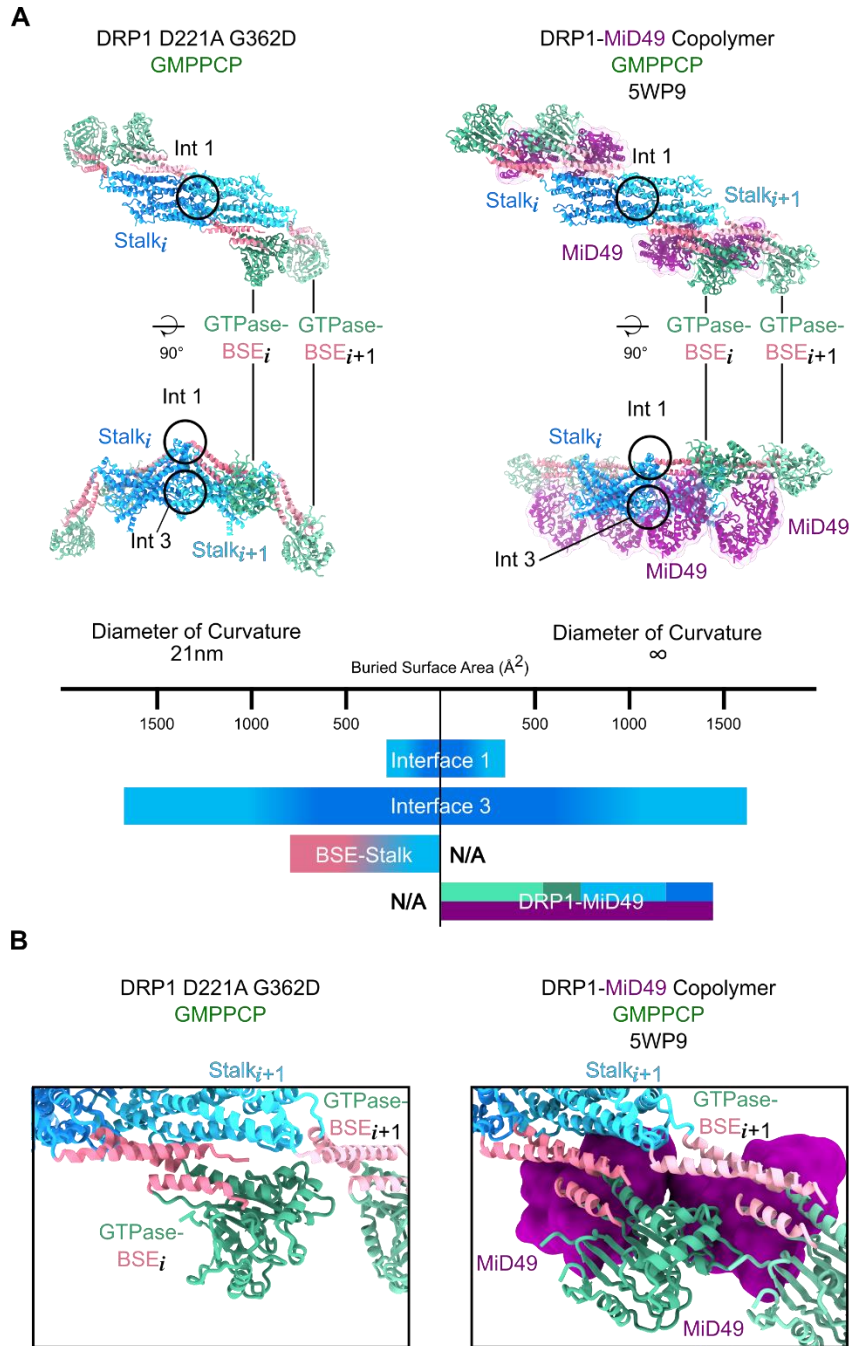


Figure 3. MiD Receptors Block a *cis*-rung Polymerization Interface between the BSE and the Stalk.

(A) Atomic model of the GMP-PCP bound DRP1 D221A G362D with a diameter of curvature of 21nm compared to the atomic model of the GMP-PCP DRP1-MiD49₁₂₆₋₄₅₄ Copolymer with an infinite diameter of curvature with domains and polymerization interfaces labeled. DRP1 is colored by domain and MiD protein is colored in purple. Comparison of changes in buried surface area between the two structures. (B) Detailed view of MiD49 wedging in between the BSE and the Stalk Domain of the next protomer in the assembly.

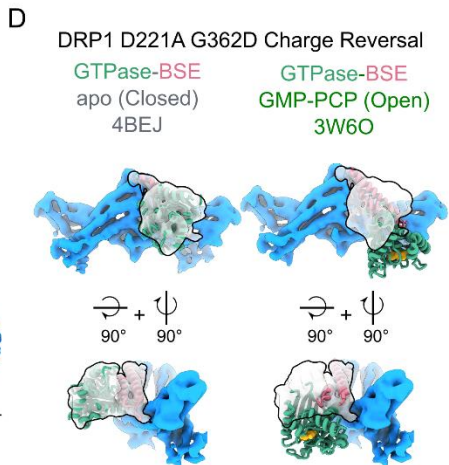
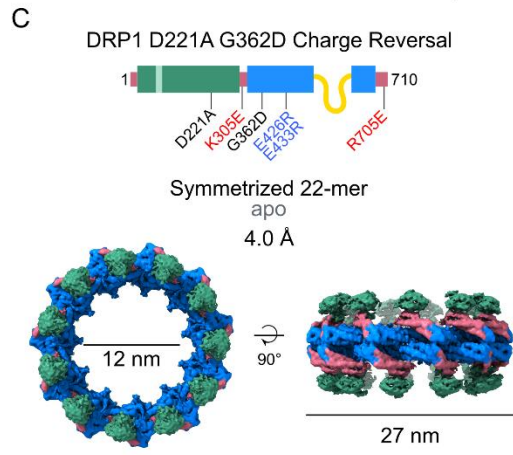
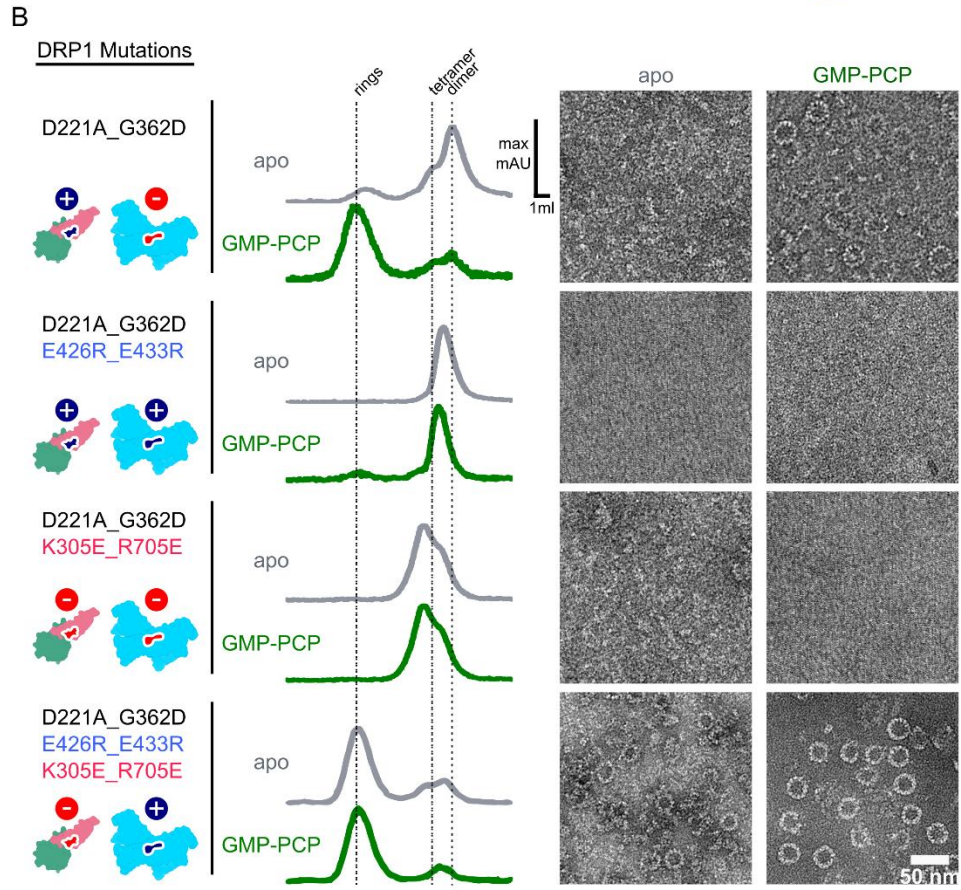
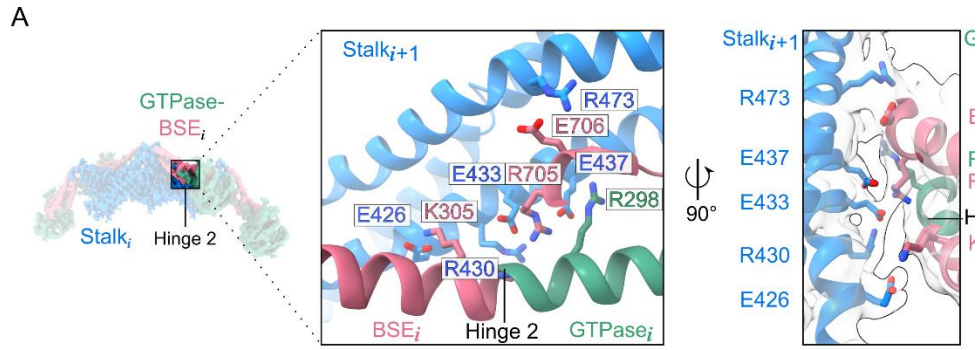
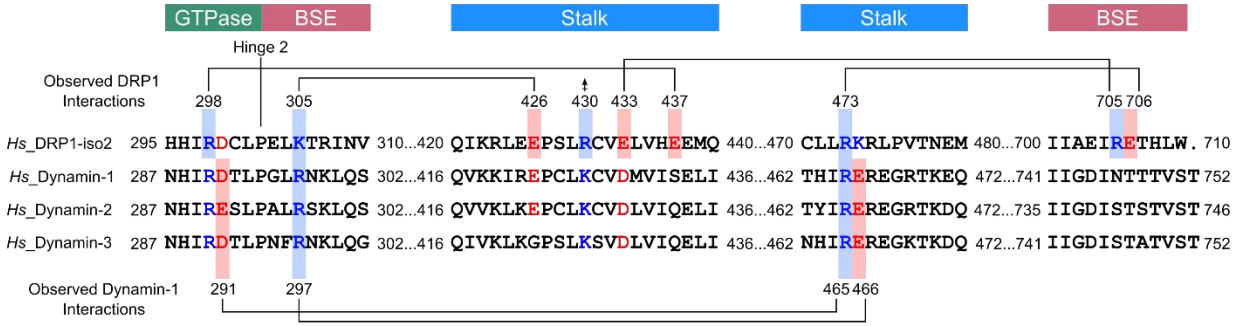


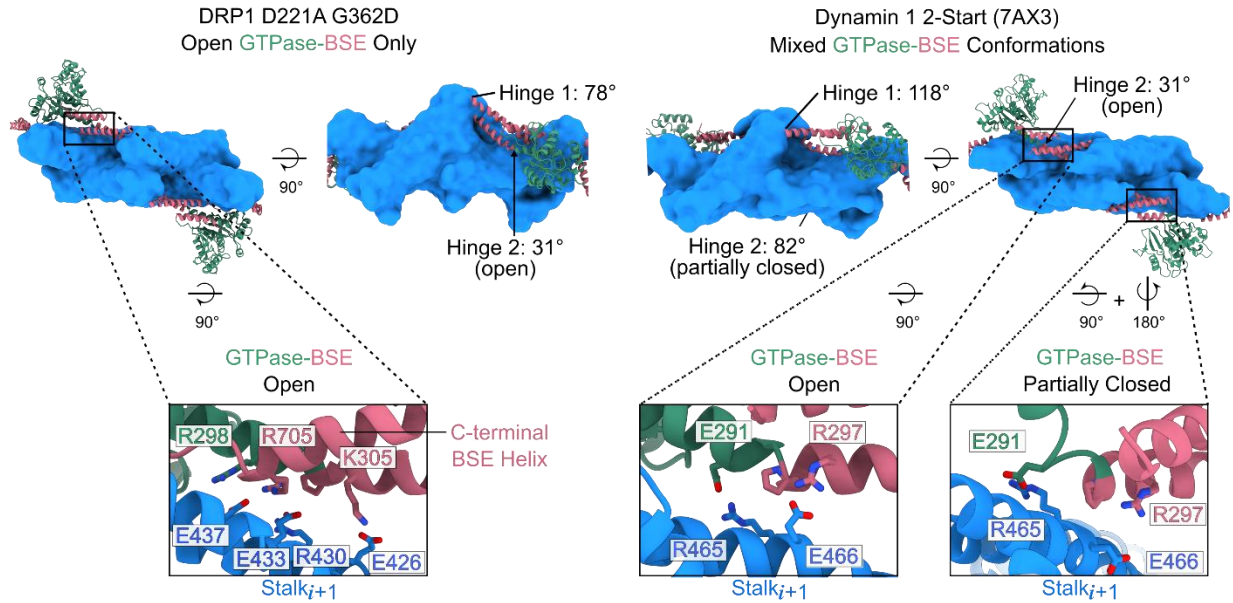
Figure 4. The BSE-Stalk Interface Is Sufficient for *cis*-rung Mediated Generation of High Curvature in the GTP state.

(A) Detailed view of the interface between the BSE and the Stalk of the next protomer in the assembly centered around the power stroke hinge 2 between the GTPase and the BSE. Residues are labeled with colors according to their respective domain. (B) Size-exclusion and negative-stain EM assay of assembly formation of charge swapped and reversal mutants at physiological ionic strength in the presence and absence of GMP-PCP in the context of the D221A G362D mutations. (C) Sequence Diagram and symmetrized cryo-EM reconstruction of the DRP1 D221A G362D Charge Reversal Mutant in the absence of nucleotide frozen at low ionic strength with density colored by respective domain. (D) Docking of atomic models of the closed (apo) GTPase-BSE domain from PDB 4BEJ and the open (GMP-PCP bound) GTPase-BSE fusion from PDB 3W6O into an unsharpened map with alignment focused on the GTPase-BSE and the nearest stalk. Docking was done based on the stronger BSE-density, with the GTPase domain showing the expected position in closed and open states.

A



B



C

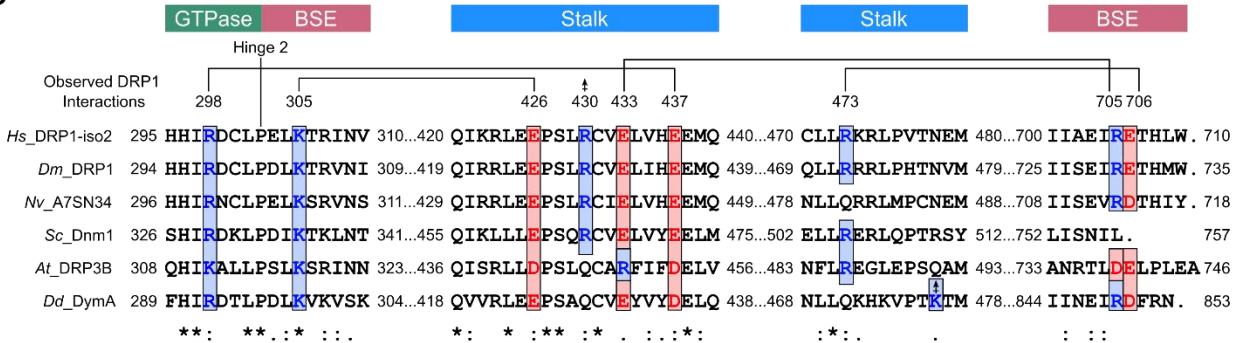


Figure S2. The C-terminal BSE Charges are Determinants of Strong *cis*-rung Constriction

(A) Conservation of sequence and BSE-Stalk interactions between *Homo sapiens* DRP1 isoform 2 and Dynamin isoforms. The GMP-PCP bound DRP1 D221A G362D structure and the GMP-PCP bound two-start dynamin 1 helix in the absence of lipid (PDB 7AX3) was used to identify BSE-Stalk interactions, but little difference exists here between it and PDB 6DLU) Amino acid letters are colored by charge and conservation of a charge-charge interaction are shown as lightly colored rectangles. In many cases the sequences appear conserved, but these interactions are not observed in cryo-EM structures. Lines indicating charge-charge pairs are shown and a dipole symbol is shown for DRP1 Arg 430. (B) Angles for Hinge 1 and Hinge 2 are shown indicating the lower (membrane proximal) binding position of the BSE on the neighboring stalk compared to Dynamin-1. Key Interactions between the BSE and the Stalk in DRP1 D221A G362D and PDB 7AX3 for each conformation of the GTPase-BSE Hinge. For clarity, the C-terminal BSE Helix of the open state of Dynamin 1 was hidden but does not interact with the Stalk domain. (C) Conservation of DRP1 ortholog sequence around the BSE-Stalk interactions with sequences from *Homo sapiens* (*Hs*), *Drosophila melanogaster* (*Dm*), the starlet sea anemone (*Nv*), *Saccharomyces cerevisiae* (*Sc*), *Arabidopsis thaliana* (*At*), and the slime mold *Dictyostelium discoideum* (*Dd*). The Uniprot accession number for *Nv* is shown in place of an ortholog name. Amino acid letters are colored by charge and conservation of a charge-charge interaction are shown as lightly colored rectangles. Lines indicating charge-charge pairs in the GMP-PCP bound DRP1 D221A G362D structure are shown. A charge reversal for *At*_DRP3B was colored as well and a dipole symbol is shown for DRP1 Arg 430 as well as *Dd*_DymA K475 as predicted in the AlphaFold 2 database.

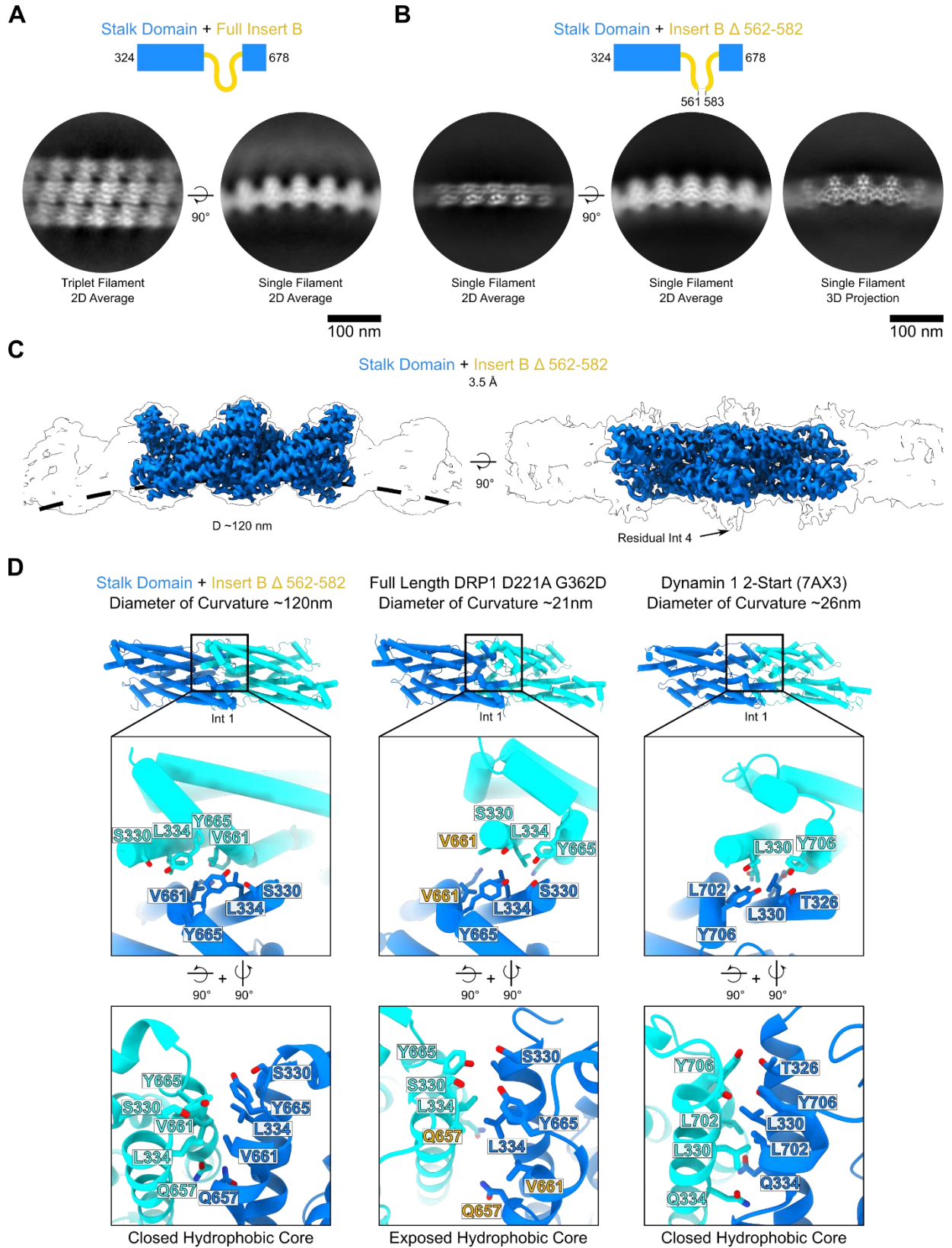


Figure 5. The Canonical Interface 1 of DRP1 is Adapted to the Low Curvature Of Mitochondria

(A) Sequence diagram and 2D averages of top views of triplet and side views of single filaments of Stalk domain with the full isoform 2 insert B in vitreous ice. (B) Sequence diagram and 2D averages of a tilted top view and a side view of the Stalk domain with isoform 2 insert B with a deletion of residues 562-582 along with a 3D side view projection of a single filament. (C) Symmetry expanded cryo-EM Map of the Stalk Domain with Insert B Δ 562-582 at a nominal resolution of 3.5Å and a diameter of curvature of 120 nm. The unmasked map at high threshold is colored as in the sequence diagram, and silhouettes are shown at low threshold. A mask of two stalks was used for alignment. Low threshold density for residual triplets is highlighted. (D) Comparison of low curvature DRP1 and high curvature DRP1 and Dynamin 1 (PDB 7AX3) interface 1 with one stalk colored in blue and the other in cyan. Residues are colored according to their domain, with the exception of V661 and Q657 in the high curvature DRP1 structure which are highlighted due to their loss of interaction at high curvature.

	Stalk			Stalk		
Observed DRP1 Interactions	334			657	661	665
Hs_DRP1-iso2	329	KSATLLQLITKF	339...655	TLOSELVGQLYKSSLL	670	
Dm_DRP1	328	KSQTLQLIITKF	338...680	NLOSELVTHLYKSDKA	695	
Nv_A7SN34	338	KGPYLLQMITRF	348...663	RIQSELVEKLYKSERF	678	
Sc_Dnm1	364	RASLVLQLMNKF	374...707	SVONRLVTKLYKETLF	722	
At_DRP3B	345	QGALLLSFITKY	355...691	ELHNVFTEKLYRENLI	706	
Dd_DynA	327	QGALLLQIITIF	337...799	HIQNELVAALYKEELF	814	
	::	::*::: ::		::: ::	**::	
Hs_Dynamin-1	325	KTKALLQMVQDF	335...696	FIFSELLANLYSCGDQ	711	
Observed Dynamain 1 Interactions	326	330	334	702	706	

Figure S3. Conservation of Interface 1 in Dynamain Proteins

Conservation of sequence around the canonical dynamain interface 1 with DRP1 ortholog sequences from Homo sapiens (Hs), Drosophila melanogaster (Dm), the starlet sea anemone Nematostella vectensis (Nv), Saccharomyces cerevisiae (Sc), Arabidopsis thaliana (At), the slime mold Dictyostelium discoideum (Dd), and Homo sapiens Hs_Dynamain-1. The Uniprot accession number for Nv is shown in place of an ortholog name. Light yellow-colored rectangles mark side chains that interact in interface 1 in the DRP1 Stalk Domain with Insert B Δ 562-582 structure and are conserved and purple rectangles mark observed dipole-dipole interactions. Similar residues were not considered conserved in this figure due to the nature of the interface but are colored golden to show their similar hydrophobicity.

Stalk Domain + Insert B Δ 562-582

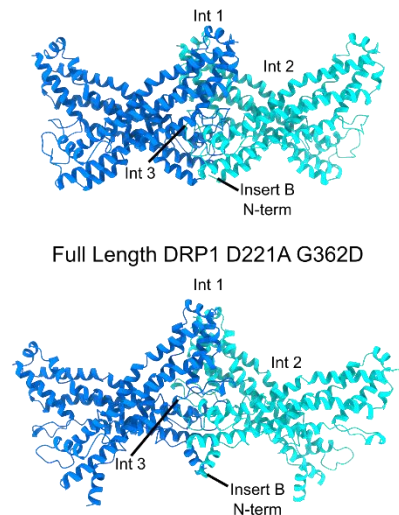


Figure S4. Interface 3 is the Fulcrum of Rotation in Curvature Generation

Two Stalk domains are shown in cartoon with one in blue and one in cyan for both the Stalk Domain with Insert B Δ 562-582 atomic model and the DRP1 D221A G362D model. Polymerization interfaces 1 and 3 are labeled along with the constitutive dimer interface 2. A conformational change of the helix N-terminal to insert B is highlighted.

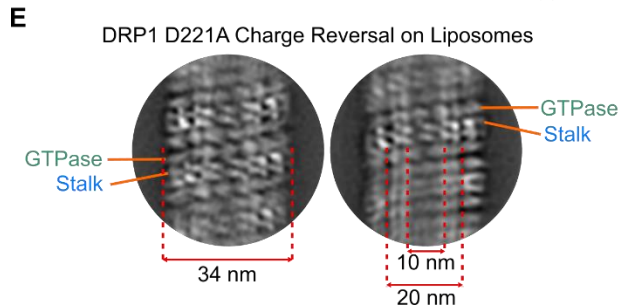
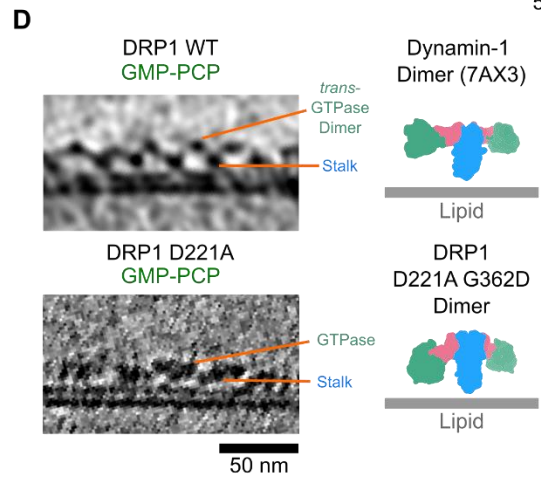
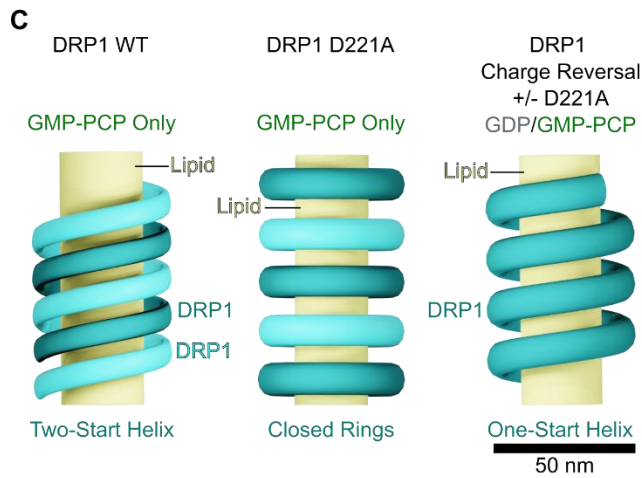
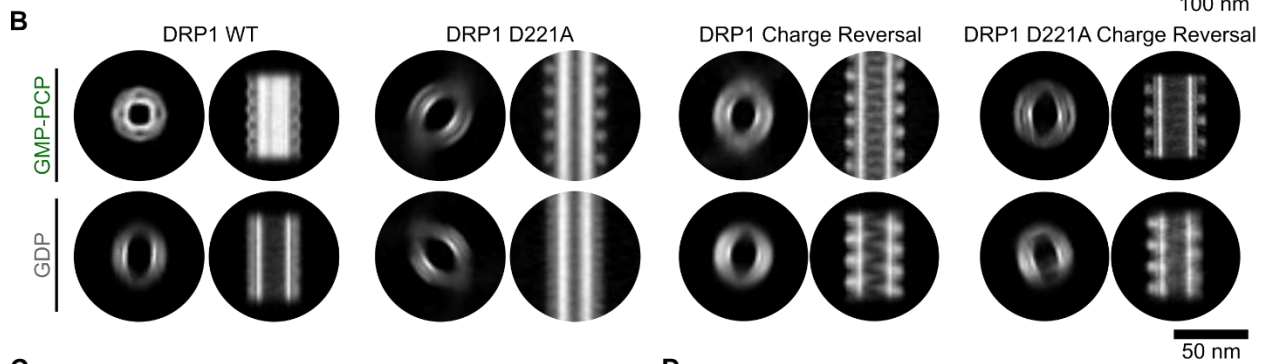
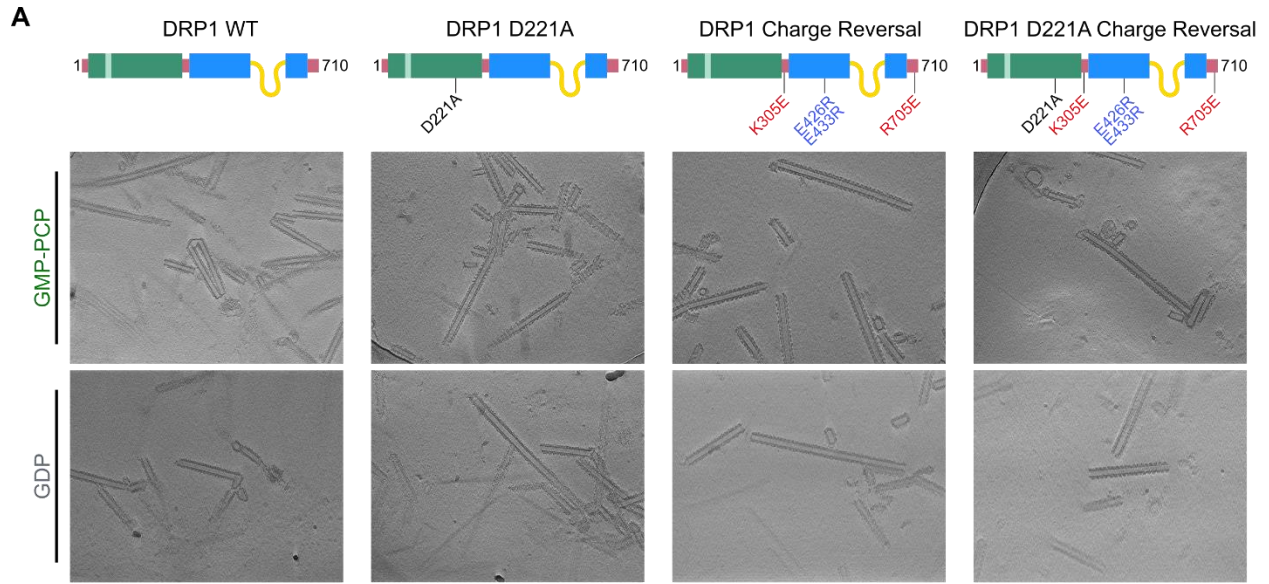


Figure 6. The BSE-Stalk Interaction is Sufficient to Constrict Lipid to Endocytic Dynamin Curvatures

(A) Representative slices of 3D electron cryo-tomograms of DRP1 isoform 2 wild type and mutants on lipid nanotubes containing anionic lipids and cardiolipin in the presence of GDP or GMP-PCP. Mutations for each construct are noted in the sequence diagram. (B) Projections of 3D subtomogram averages of DRP1 isoform 2 wild type and mutants in the presence of GDP or GMP-PCP. (C) 3D Generated models of the helical parameters or ring spacing of DRP1 isoform 2 wild type and D221A in the presence of GMP-PCP and the charge reversal mutant with and without the D221A mutation and with GDP or GMP-PCP. (D) A thin projection slice of the subtomogram average of GMP-PCP bound DRP1 wild type and D221A on lipid nanotubes. *Trans*-GTPase dimers are highlighted in the wild type slice and the flat projection of the atomic model interface 1 dimer for 7AX3 and DRP1 D221A G362D is shown by its side for comparison colored by domain to show the relative position of GTPase domains. (E) 2D Average of the DRP1 D221A charge reversal mutant tubulating liposomes to an inner luminal diameter of 10 nm and outer leaflet diameter of 20 nm in the absence of nucleotide.

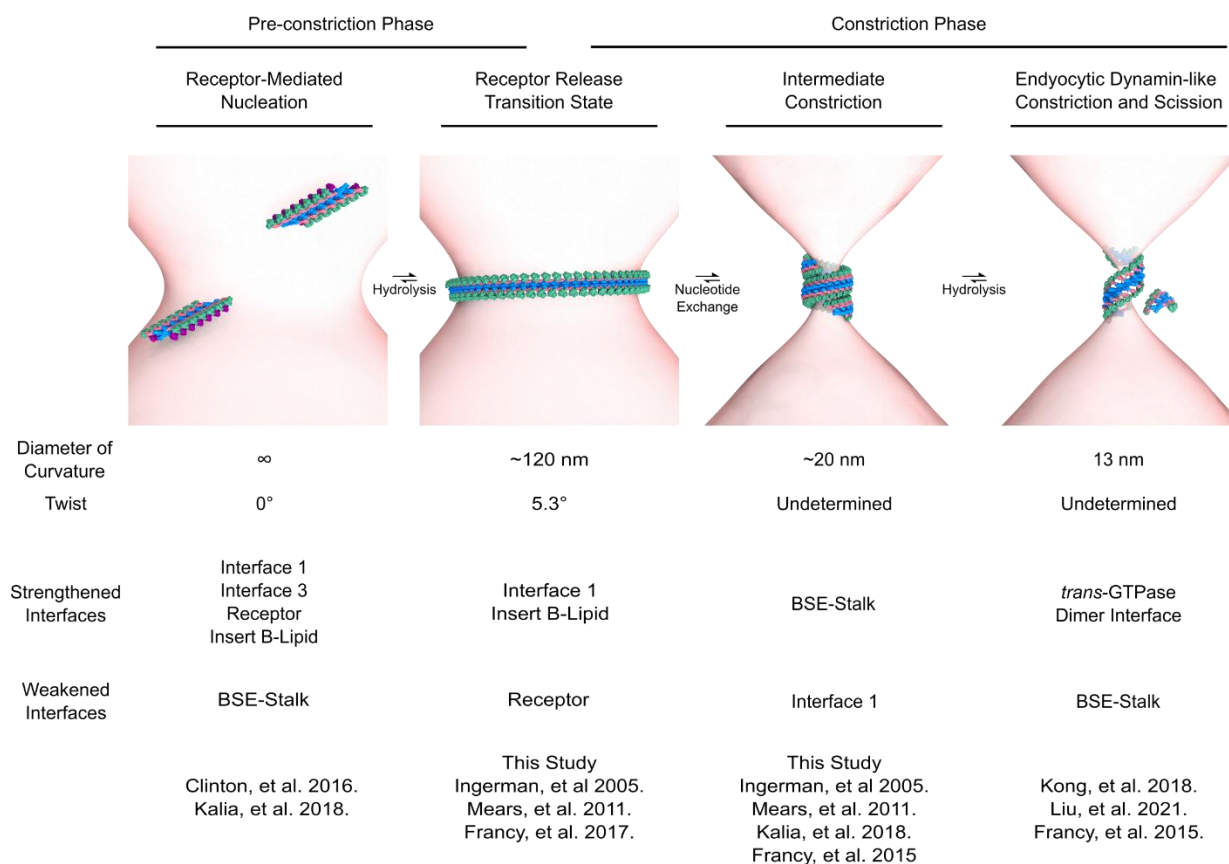


Figure 7. A Model for DRP1 Constriction of Low Curvature Membranes

Protein models are colored with the GTPase domain in green, BSE in pink, Stalk Domain in blue, and MiD49 in purple. A seven-dimer model of PDB 5WP9 is shown after receptor-mediated nucleation on a simulated outer mitochondrial membrane showing a pre-constriction of ~130nm to scale. The atomic model is placed as close as possible to the pre-constriction site without having a side of the polymer deviate far from the membrane. After receptor release, a 30 dimer model of the Stalk from the Stalk Domain with Insert B Δ 562-582 is shown with the closed (apo) GTPase-BSE from PDB 4BEJ. Curvature parameters from the map are shown to scale, but an imagined helical rise is shown such that it does not close. After an intermediate constriction, A 30-dimer model of the GMP-PCP bound DRP1 D221A G362D model is shown with curvature to scale, but a helical rise is shown which matches the rise of the tabulated liposome sample. After further hydrolysis and endocytic dynamin-like constriction and hemfission of the outer mitochondrial membrane, pieces of GMP-PCP bound DRP1 D221A G362D are still shown as structural observation of this state remains elusive. The curvatures and interfaces that must be strengthened and weakened at each step are listed, along with citations that support the curvature and existence of each state.

References

- Antonny, B., Burd, C., De Camilli, P., Chen, E., Daumke, O., Faelber, K., Ford, M., Frolov, V. A., Frost, A., Hinshaw, J. E., Kirchhausen, T., Kozlov, M. M., Lenz, M., Low, H. H., McMahon, H., Merrifield, C., Pollard, T. D., Robinson, P. J., Roux, A., & Schmid, S. (2016). Membrane fission by dynamin: What we know and what we need to know. *The EMBO Journal*, *35*(21), 2270–2284. <https://doi.org/10.15252/emj.201694613>
- Asarnow, D., Palovcak, E., & Cheng, Y. (2019). *asarnow/pyem: UCSF pyem v0.5*. Zenodo. <https://doi.org/10.5281/zenodo.3576630>
- Bustillo-Zabalbeitia, I., Montessuit, S., Raemy, E., Basañez, G., Terrones, O., & Martinou, J.-C. (2014). Specific Interaction with Cardiolipin Triggers Functional Activation of Dynamin-Related Protein 1. *PLOS ONE*, *9*(7), e102738. <https://doi.org/10.1371/journal.pone.0102738>
- Chappie, J. S., Acharya, S., Leonard, M., Schmid, S. L., & Dyda, F. (2010). G domain dimerization controls dynamin's assembly-stimulated GTPase activity. *Nature*, *465*(7297), 435–440. <https://doi.org/10.1038/nature09032>
- Chappie, J. S., Mears, J. A., Fang, S., Leonard, M., Schmid, S. L., Milligan, R. A., Hinshaw, J. E., & Dyda, F. (2011). A Pseudoatomic Model of the Dynamin Polymer Identifies a Hydrolysis-Dependent Powerstroke. *Cell*, *147*(1), 209–222. <https://doi.org/10.1016/j.cell.2011.09.003>
- Chen, X., Xu, X., Sun, Y., Zhou, J., Ma, Y., Yan, L., & Lou, Z. (2012). Purification, crystallization and preliminary X-ray crystallographic analysis of Arabidopsis thaliana dynamin-related protein 1A GTPase-GED fusion protein. *Acta Crystallographica Section F*, *68*(1), 69–72. <https://doi.org/10.1107/S1744309111047634>

Clinton, R. W., Francy, C. A., Ramachandran, R., Qi, X., & Mears, J. A. (2016). Dynamin-related Protein 1 Oligomerization in Solution Impairs Functional Interactions with Membrane-anchored Mitochondrial Fission Factor. *Journal of Biological Chemistry*, 291(1), 478–492. <https://doi.org/10.1074/jbc.M115.680025>

Cocucci, E., Gaudin, R., & Kirchhausen, T. (2014). Dynamin recruitment and membrane scission at the neck of a clathrin-coated pit. *Molecular Biology of the Cell*, 25(22), 3595–3609. <https://doi.org/10.1091/mbc.e14-07-1240>

Croll, T. I. (2018). ISOLDE: A physically realistic environment for model building into low-resolution electron-density maps. *Acta Crystallographica. Section D, Structural Biology*, 74(Pt 6), 519–530. <https://doi.org/10.1107/S2059798318002425>

Danino, D., Moon, K.-H., & Hinshaw, J. E. (2004). Rapid constriction of lipid bilayers by the mechanochemical enzyme dynamin. *Journal of Structural Biology*, 147(3), 259–267. <https://doi.org/10.1016/j.jsb.2004.04.005>

Emsley, P., & Cowtan, K. (2004). Coot: Model-building tools for molecular graphics. *Acta Crystallographica Section D: Biological Crystallography*, 60(12), 2126–2132. <https://doi.org/10.1107/S0907444904019158>

Emsley, P., Lohkamp, B., Scott, W. G., & Cowtan, K. (2010). Features and development of Coot. *Acta Crystallographica Section D: Biological Crystallography*, 66(4), 486–501. <https://doi.org/10.1107/S0907444910007493>

Ferguson, S., Raimondi, A., Paradise, S., Shen, H., Mesaki, K., Ferguson, A., Destaing, O., Ko, G., Takasaki, J., Cremona, O., Toole, E. O., & Camilli, P. D. (2009). Coordinated Actions of

Actin and BAR Proteins Upstream of Dynamin at Endocytic Clathrin-Coated Pits. *Developmental Cell*, 17(6), 811–822. <https://doi.org/10.1016/j.devcel.2009.11.005>

Figuroa-Romero, C., Iñiguez-Lluhí, J. A., Stadler, J., Chang, C.-R., Arnoult, D., Keller, P. J., Hong, Y., Blackstone, C., & Feldman, E. L. (2009). SUMOylation of the mitochondrial fission protein Drp1 occurs at multiple nonconsensus sites within the B domain and is linked to its activity cycle. *The FASEB Journal*, 23(11), 3917–3927. <https://doi.org/10.1096/fj.09-136630>

Francy, C. A., Clinton, R. W., Fröhlich, C., Murphy, C., & Mears, J. A. (2017). Cryo-EM Studies of Drp1 Reveal Cardiolipin Interactions that Activate the Helical Oligomer. *Scientific Reports*, 7(1), 10744. <https://doi.org/10.1038/s41598-017-11008-3>

Friedman, J. R., Lackner, L. L., West, M., DiBenedetto, J. R., Nunnari, J., & Voeltz, G. K. (2011). ER Tubules Mark Sites of Mitochondrial Division. *Science*, 334(6054), 358–362. <https://doi.org/10.1126/science.1207385>

Fröhlich, C., Grabiger, S., Schwefel, D., Faelber, K., Rosenbaum, E., Mears, J., Rocks, O., & Daumke, O. (2013). Structural insights into oligomerization and mitochondrial remodelling of dynamin 1-like protein. *The EMBO Journal*, 32(9), 1280–1292. <https://doi.org/10.1038/emboj.2013.74>

Ganichkin, O. M., Vancraenenbroeck, R., Rosenblum, G., Hofmann, H., Mikhailov, A. S., Daumke, O., & Noel, J. K. (2021). Quantification and demonstration of the collective constriction-by-ratchet mechanism in the dynamin molecular motor. *Proceedings of the National Academy of Sciences of the United States of America*, 118(28), e2101144118. <https://doi.org/10.1073/pnas.2101144118>

Goddard, T. D., Huang, C. C., Meng, E. C., Pettersen, E. F., Couch, G. S., Morris, J. H., & Ferrin, T. E. (2018). UCSF ChimeraX: Meeting modern challenges in visualization and analysis. *Protein Science: A Publication of the Protein Society*, 27(1), 14–25. <https://doi.org/10.1002/pro.3235>

Grant, T., Rohou, A., & Grigorieff, N. (2018). CisTEM, user-friendly software for single-particle image processing. *ELife*, 7, e35383. <https://doi.org/10.7554/eLife.35383>

Helle, S. C. J., Feng, Q., Aebersold, M. J., Hirt, L., Grüter, R. R., Vahid, A., Sirianni, A., Mostowy, S., Snedeker, J. G., Šarić, A., Idema, T., Zambelli, T., & Kornmann, B. (2017). Mechanical force induces mitochondrial fission. *ELife*, 6, e30292. <https://doi.org/10.7554/eLife.30292>

Ingerman, E., Perkins, E. M., Marino, M., Mears, J. A., McCaffery, J. M., Hinshaw, J. E., & Nunnari, J. (2005). Dnm1 forms spirals that are structurally tailored to fit mitochondria. *The Journal of Cell Biology*, 170(7), 1021–1027. <https://doi.org/10.1083/jcb.200506078>

Kalia, R., Wang, R. Y.-R., Yusuf, A., Thomas, P. V., Agard, D. A., Shaw, J. M., & Frost, A. (2018). Structural basis of mitochondrial receptor binding and constriction by DRP1. *Nature*, 558(7710), 401–405. <https://doi.org/10.1038/s41586-018-0211-2>

Kishida, H., & Sugio, S. (2013). Crystal structure of GTPase domain fused with minimal stalks from human dynamin-1-like protein (Dlpl) in complex with several nucleotide analogues. *Current Topics in Peptide and Protein Research*, 14, 67–77.

Kong, L., Sochacki, K. A., Wang, H., Fang, S., Canagarajah, B., Kehr, A. D., Rice, W. J., Strub, M.-P., Taraska, J. W., & Hinshaw, J. E. (2018). Cryo-EM of the dynamin polymer assembled on lipid membrane. *Nature*, 560(7717), 258–262. <https://doi.org/10.1038/s41586-018-0378-6>

- Krissinel, E., & Henrick, K. (2007). Inference of Macromolecular Assemblies from Crystalline State. *Journal of Molecular Biology*, 372(3), 774–797. <https://doi.org/10.1016/j.jmb.2007.05.022>
- Liebschner, D., Afonine, P. V., Baker, M. L., Bunkóczi, G., Chen, V. B., Croll, T. I., Hintze, B., Hung, L.-W., Jain, S., McCoy, A. J., Moriarty, N. W., Oeffner, R. D., Poon, B. K., Prisant, M. G., Read, R. J., Richardson, J. S., Richardson, D. C., Sammito, M. D., Sobolev, O. V., ... Adams, P. D. (2019). Macromolecular structure determination using X-rays, neutrons and electrons: Recent developments in Phenix. *Acta Crystallographica Section D: Structural Biology*, 75(10), 861–877. <https://doi.org/10.1107/S2059798319011471>
- Liu, J., Alvarez, F. J. D., Clare, D. K., Noel, J. K., & Zhang, P. (2021). CryoEM structure of the super-constricted two-start dynamin 1 filament. *Nature Communications*, 12(1), 5393. <https://doi.org/10.1038/s41467-021-25741-x>
- Liu, R., & Chan, D. C. (2015). The mitochondrial fission receptor Mff selectively recruits oligomerized Drp1. *Molecular Biology of the Cell*, 26(24), 4466–4477. <https://doi.org/10.1091/mbc.E15-08-0591>
- Losón, O. C., Song, Z., Chen, H., & Chan, D. C. (2013). Fis1, Mff, MiD49, and MiD51 mediate Drp1 recruitment in mitochondrial fission. *Molecular Biology of the Cell*, 24(5), 659–667. <https://doi.org/10.1091/mbc.E12-10-0721>
- Lu, B., Kennedy, B., Clinton, R. W., Wang, E. J., McHugh, D., Stepanyants, N., Macdonald, P. J., Mears, J. A., Qi, X., & Ramachandran, R. (2018). Steric interference from intrinsically disordered regions controls dynamin-related protein 1 self-assembly during mitochondrial fission. *Scientific Reports*, 8(1), 10879. <https://doi.org/10.1038/s41598-018-29001-9>

Macdonald, P. J., Francy, C. A., Stepanyants, N., Lehman, L., Baglio, A., Mears, J. A., Qi, X., & Ramachandran, R. (2015). Distinct Splice Variants of Dynamin-related Protein 1 Differentially Utilize Mitochondrial Fission Factor as an Effector of Cooperative GTPase Activity. *Journal of Biological Chemistry*, jbc.M115.680181. <https://doi.org/10.1074/jbc.M115.680181>

Mahajan, M., Bharambe, N., Shang, Y., Lu, B., Mandal, A., Mohan, P. M., Wang, R., Boatz, J. C., Galvez, J. M. M., Shnyrova, A. V., Qi, X., Buck, M., Wel, P. C. A. van der, & Ramachandran, R. (2021). NMR identification of a conserved Drp1 cardiolipin-binding motif essential for stress-induced mitochondrial fission. *Proceedings of the National Academy of Sciences*, 118(29). <https://doi.org/10.1073/pnas.2023079118>

Mears, J. A., Lackner, L. L., Fang, S., Ingerman, E., Nunnari, J., & Hinshaw, J. E. (2011). Conformational changes in Dnm1 support a contractile mechanism for mitochondrial fission. *Nature Structural & Molecular Biology*, 18(1), 20–26. <https://doi.org/10.1038/nsmb.1949>

Park, R. J., Shen, H., Liu, L., Liu, X., Ferguson, S. M., & De Camilli, P. (2013). Dynamin triple knockout cells reveal off target effects of commonly used dynamin inhibitors. *Journal of Cell Science*, 126(22), 5305–5312. <https://doi.org/10.1242/jcs.138578>

Pettersen, E. F., Goddard, T. D., Huang, C. C., Meng, E. C., Couch, G. S., Croll, T. I., Morris, J. H., & Ferrin, T. E. (2021). UCSF ChimeraX: Structure visualization for researchers, educators, and developers. *Protein Science: A Publication of the Protein Society*, 30(1), 70–82. <https://doi.org/10.1002/pro.3943>

Punjani, A., Rubinstein, J. L., Fleet, D. J., & Brubaker, M. A. (2017). cryoSPARC: Algorithms for rapid unsupervised cryo-EM structure determination. *Nature Methods*, 14(3), 290–296. <https://doi.org/10.1038/nmeth.4169>

Ramachandran, R., & Schmid, S. L. (2018). The dynamin superfamily. *Current Biology*, 28(8), R411–R416. <https://doi.org/10.1016/j.cub.2017.12.013>

Reubold, T. F., Faelber, K., Plattner, N., Posor, Y., Ketel, K., Curth, U., Schlegel, J., Anand, R., Manstein, D. J., Noé, F., Haucke, V., Daumke, O., & Eschenburg, S. (2015). Crystal structure of the dynamin tetramer. *Nature*, 525(7569), 404–408. <https://doi.org/10.1038/nature14880>

Schmid, E. M., & McMahon, H. T. (2007). Integrating molecular and network biology to decode endocytosis. *Nature*, 448(7156), 883–888. <https://doi.org/10.1038/nature06031>

Schorb, M., Haberbosch, I., Hagen, W. J. H., Schwab, Y., & Mastronarde, D. N. (2019). Software tools for automated transmission electron microscopy. *Nature Methods*, 16(6), 471–477. <https://doi.org/10.1038/s41592-019-0396-9>

Schrödinger, LLC. (2015). *The PyMOL Molecular Graphics System, Version 1.8*.

Sugiura, A., Mattie, S., Prudent, J., & McBride, H. M. (2017). Newly born peroxisomes are a hybrid of mitochondrial and ER-derived pre-peroxisomes. *Nature*, 542(7640), 251–254. <https://doi.org/10.1038/nature21375>

Sweitzer, S. M., & Hinshaw, J. E. (1998). Dynamin Undergoes a GTP-Dependent Conformational Change Causing Vesiculation. *Cell*, 93(6), 1021–1029. [https://doi.org/10.1016/S0092-8674\(00\)81207-6](https://doi.org/10.1016/S0092-8674(00)81207-6)

Takeda, T., Kozai, T., Yang, H., Ishikuro, D., Seyama, K., Kumagai, Y., Abe, T., Yamada, H., Uchihashi, T., Ando, T., & Takei, K. (n.d.). Dynamic clustering of dynamin-amphiphysin helices regulates membrane constriction and fission coupled with GTP hydrolysis. *ELife*, 7, e30246. <https://doi.org/10.7554/eLife.30246>

Takei, K., Haucke, V., Slepnev, V., Farsad, K., Salazar, M., Chen, H., & Camilli, P. D. (1998). Generation of Coated Intermediates of Clathrin-Mediated Endocytosis on Protein-Free Liposomes. *Cell*, *94*(1), 131–141. [https://doi.org/10.1016/S0092-8674\(00\)81228-3](https://doi.org/10.1016/S0092-8674(00)81228-3)

Takei, K., Slepnev, V. I., Haucke, V., & De Camilli, P. (1999). Functional partnership between amphiphysin and dynamin in clathrin-mediated endocytosis. *Nature Cell Biology*, *1*(1), 33–39. <https://doi.org/10.1038/9004>

Tristan Croll. (2021, May 3). <—(Developer of ISOLDE) Depends on your application. If you intend to deposit to the wwPDB, then refinement (in your choice of Phenix or REFMAC) is pretty much mandatory. Biggest reason: ISOLDE doesn't refine B-factors. (1/9) [Tweet]. @CrollTristan. <https://twitter.com/CrollTristan/status/1389284393106255876>

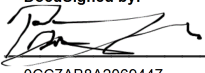
Zivanov, J., Nakane, T., Forsberg, B. O., Kimanius, D., Hagen, W. J., Lindahl, E., & Scheres, S. H. (2018). New tools for automated high-resolution cryo-EM structure determination in RELION-3. *ELife*, *7*, e42166. <https://doi.org/10.7554/eLife.42166>

Zivanov, J., Nakane, T., & Scheres, S. H. W. (2020). Estimation of high-order aberrations and anisotropic magnification from cryo-EM data sets in RELION-3.1. *IUCrJ*, *7*(2), 253–267. <https://doi.org/10.1107/S2052252520000081>

Publishing Agreement

It is the policy of the University to encourage open access and broad distribution of all theses, dissertations, and manuscripts. The Graduate Division will facilitate the distribution of UCSF theses, dissertations, and manuscripts to the UCSF Library for open access and distribution. UCSF will make such theses, dissertations, and manuscripts accessible to the public and will take reasonable steps to preserve these works in perpetuity.

I hereby grant the non-exclusive, perpetual right to The Regents of the University of California to reproduce, publicly display, distribute, preserve, and publish copies of my thesis, dissertation, or manuscript in any form or media, now existing or later derived, including access online for teaching, research, and public service purposes.

DocuSigned by:

0CC7AB8A2069447... Author Signature

3/8/2022
Date